

# First-Principles Momentum Dependent Local Ansatz Approach to the Momentum Distribution Function in Iron-Group Transition Metals

Yoshiro Kakehashi\* and Sumal Chandra

*Department of Physics and Earth Sciences, Faculty of Science,  
University of the Ryukyus,  
1 Senbaru, Nishihara, Okinawa, 903-0213, Japan*

The momentum distribution function (MDF) bands of iron-group transition metals from Sc to Cu have been investigated on the basis of the first-principles momentum dependent local ansatz wavefunction method. It is found that the MDF for  $d$  electrons show a strong momentum dependence and a large deviation from the Fermi-Dirac distribution function along high-symmetry lines of the first Brillouin zone, while the  $sp$  electrons behave as independent electrons. In particular, the deviation in bcc Fe (fcc Ni) is shown to be enhanced by the narrow  $e_g$  ( $t_{2g}$ ) bands with flat dispersion in the vicinity of the Fermi level. Mass enhancement factors (MEF) calculated from the jump on the Fermi surface are also shown to be momentum dependent. Large mass enhancements of Mn and Fe are found to be caused by spin fluctuations due to  $d$  electrons, while that for Ni is mainly caused by charge fluctuations. Calculated MEF are consistent with electronic specific heat data as well as the recent angle resolved photoemission spectroscopy data.

**KEYWORDS:** first-principles variational theory, momentum-dependent local ansatz, iron-group transition metals, electron correlations, momentum distribution function, mass enhancement factor

## 1. Introduction

The iron-group transition metals and compounds show a variety of physical properties such as anomalous cohesive properties,<sup>1)</sup> appearance of the ferro- and antiferro-magnetism,<sup>2,3)</sup> and high- $T_c$  superconductivity.<sup>4)</sup> Many of their electronic, cohesive, and magnetic properties are well-known to be explained quantitatively by the density functional band theory (DFT).<sup>5–10)</sup>

The DFT is based on the Hohenberg-Kohn theorem which states that the ground state is given by the functional of electron density and the Kohn-Sham scheme which makes use of the density of an independent electron system. With use of the exchange-correlation potential in the local density approximation (LDA)<sup>11)</sup> or the generalized gradient approximation (GGA),<sup>12,13)</sup> the DFT quantitatively explained the stability of the structure and magnetism, the lattice parameter, the bulk modulus, as well as the magnetism in transition metals and compounds.<sup>8–10)</sup>

---

\*yok@sci.u-ryukyu.ac.jp, to be published in J. Phys. Soc. Jpn. (2017).

Although the DFT has been successful in quantitative description of the physical properties of many metals and compounds, problems and limitations of the DFT have also been clarified over the past five decades. One of the serious problems is that the quantitative aspects of the DFT become unstable with increasing Coulomb interaction strength. The DFT, for example, fails to explain the paramagnetism in  $\epsilon$ -Fe,<sup>14)</sup> the weak antiferromagnetism in Fe-pnictides,<sup>4)</sup> as well as the antiferromagnetism in cuprates.<sup>2)</sup> The problem limits the application range of the DFT. The second problem is that excited states and related excitation spectra cannot be described by the DFT because the latter is based on the Hohenberg-Kohn theorem. For the same reason, the physical quantities such as the charge and spin fluctuations described by the two-particle operators cannot be obtained by the DFT. Finally, the momentum distribution function and related mass enhancement factor cannot be obtained by the DFT because the DFT is based on the Kohn-Sham scheme.

Because of the problems and limitations of the DFT mentioned above, the ground-state properties and related excitations of iron-group transition metals have not yet been fully understood from the quantitative point of view. In order to clarify the properties, we have to take alternative approaches such as the Gutzwiller wavefunction method<sup>15–20)</sup> and the dynamical mean field theory (DMFT),<sup>21,22)</sup> or equivalently the dynamical coherent potential approximation (DCPA).<sup>3,23–25)</sup> Using the first-principles DCPA, we recently performed the calculations of single-particle excitation spectra from Sc to Cu at finite temperatures, and elucidated the systematic change of the XPS spectra of iron-group transition metals.<sup>24)</sup>

For the quantitative description of the ground-state properties, the wavefunction method is useful.<sup>2,26)</sup> The first-principles Gutzwiller theory can resolve a small energy difference between the states at zero temperature which is not achieved by the first-principles DMFT. But it does not yield the correct weak Coulomb interaction limit. In order to describe quantitatively the ground-state properties of correlated electrons, we have recently proposed the momentum dependent local ansatz (MLA) theory<sup>20,27–29)</sup> which goes beyond the Gutzwiller wavefunction method.<sup>15,16)</sup> The MLA takes into account all the two-particle excited states with momentum-dependent variational amplitudes, so that the theory reduces to the Rayleigh-Schrödinger perturbation theory in the weak Coulomb interaction limit and describes well correlated electrons from the weak to strong Coulomb interaction regime. In particular, the MLA describes quantitatively the momentum distribution function in contradiction to the case of the Gutzwiller wavefunction.

Quit recently, we extended the MLA to the first-principles version combining the theory with the first-principles tight-binding LDA+U Hamiltonian.<sup>30,31)</sup> On the basis of the first principles MLA, we calculated the correlation energy, charge fluctuations, amplitude of local moment, and the momentum distribution function for paramagnetic iron, and clarified the ground-state property.<sup>31)</sup> Subsequently, we investigated the correlation energy, charge

fluctuations, and the amplitude of local moment of the iron-group transition metals in the paramagnetic state using the same theory, and clarified the correlation effects on these quantities.<sup>32)</sup>

In this paper, we investigate the momentum distribution functions (MDF) and mass enhancement factors (MEF) of the iron-group transition metals from Sc to Cu on the basis of the first-principles MLA in order to understand their systematic change over the  $3d$  series. The MDF is the simplest static quantity which cannot be described by the DFT and the simplest one-particle quantity indicating the strength of electron correlations. It also provides us with a Fermi liquid parameter of the system, *i.e.*, the MEF, from the jump at the Fermi surface. Present work is the first systematic investigations for the change of the band structure of the MDF and the MEF in iron-group transition metals at zero temperature. We will demonstrate that the MDF bands for  $d$  electrons in Mn, Fe, Co, and Ni strongly deviate from the Fermi-Dirac distribution function due to electron correlations. These deviations yield significant MEF which cannot be explained by the DFT.

We remark that the first-principles MLA is competitive with the first-principles DMFT (*i.e.*, DCPA)<sup>3, 21–25)</sup> for the calculation of the properties at zero temperature. The DMFT is a powerful method to strongly correlated electrons and has been applied to many systems. The accuracy of the DMFT however strongly depends on the solver of the impurity problem for correlated electrons. The Quantum Monte-Carlo method (QMC) can describe accurately the finite-temperature properties of the system. But its efficiency is strongly reduced at low temperatures, and the QMC even causes the negative sign problem which prevents us from systematic investigations over wide range of interaction parameters. The exact diagonalization method (ED) is useful to study exactly the physical properties at zero temperature. But it cannot describe the low energy properties associated with the Fermi surface. The numerical renormalization group theory (NRG) can describe accurately the low energy excitations, but it does not accurately describe the excitations in high-energy region as well as the energy-integrated quantities. Furthermore it is not applicable to the realistic systems because of the numerical difficulty.

The MLA describes quantitatively the quasi-particle weight associated with the low energy excitations as well as the energy-integrated quantities such as the total energy and momentum distribution function without numerical difficulty. In particular, we have shown in the recent paper<sup>30)</sup> that the first-principles MLA quantitatively explains the mass enhancement factor of bcc Fe obtained by the ARPES experiment, while the LDA+DMFT combined with the three-body theory at zero temperature does not.<sup>33)</sup> Furthermore it also allows us to calculate any static physical quantity because the wavefunction is known. These facts indicate that the first-principles MLA is suitable for the quantitative investigations of correlated electrons at zero temperature.

In the following section, we outline the first-principles MLA. We present the MLA wavefunction with three kinds of correlators for the first-principles LDA+U Hamiltonian, and obtain the ground-state energy in the single-site approximation (SSA). Next, we derive the self-consistent equations for variational parameters from the ground-state energy. In §3, we present the MDF calculated along high-symmetry lines in the first Brillouin zone. We demonstrate that the MDF for  $d$  electrons show a large deviations from the Fermi distribution function for Mn, Fe, Co, and Ni due to electron correlations. Accordingly, the MEF show significantly large values from 1.2 to 1.7. Calculated MEF are consistent with those obtained from the electronic specific heat and angle resolved photoemission spectroscopy (ARPES) data. We will clarify the role of electron correlations in the MDF and MEF from Sc to Cu as well as the role of  $s$ ,  $p$ , and  $d$  electrons in the MDF and the MEF. In the last section we summarize our results and discuss the effects of magnetism on the MEF.

## 2. First-Principles MLA

We adopt the first-principles LDA+U Hamiltonian with an atom in the unit cell.<sup>3,22)</sup>

$$H = \sum_{iL\sigma} \epsilon_L^0 n_{iL\sigma} + \sum_{iLjL'\sigma} t_{iLjL'} a_{iL\sigma}^\dagger a_{jL'\sigma} + \sum_i \left[ \sum_m U_{mm} n_{ilm\uparrow} n_{ilm\downarrow} + \sum_{(m,m')} \left( U_{mm'} - \frac{1}{2} J_{mm'} \right) n_{ilm} n_{ilm'} - 2 \sum_{(m,m')} J_{mm'} \mathbf{s}_{ilm} \cdot \mathbf{s}_{ilm'} \right]. \quad (1)$$

Here  $\epsilon_L^0$  is an atomic level of orbital  $L$  on site  $i$ .  $t_{iLjL'}$  is a transfer integral between  $iL$  and  $jL'$ ,  $L = (l, m)$  being the  $s$  ( $l = 0$ ),  $p$  ( $l = 1$ ), and  $d$  ( $l = 2$ ) orbitals.<sup>34,35)</sup>  $a_{iL\sigma}^\dagger$  ( $a_{iL\sigma}$ ) is the creation (annihilation) operator for an electron on site  $i$  with orbital  $L$  and spin  $\sigma$ , and  $n_{iL\sigma} = a_{iL\sigma}^\dagger a_{iL\sigma}$  is the number operator on the same site  $i$  with orbital  $L$  and spin  $\sigma$ . The atomic level  $\epsilon_L^0$  is calculated from the LDA atomic level  $\epsilon_L$  by subtracting the double counting potential.<sup>22)</sup> The third term at the rhs (right-hand-side) of Eq. (1) denotes the on-site Coulomb interactions between  $d$  electrons.  $U_{mm}$  ( $U_{mm'}$ ) and  $J_{mm'}$  are the intra-orbital (inter-orbital) Coulomb and exchange interactions between  $d$  electrons, respectively.  $n_{ilm}$  ( $\mathbf{s}_{ilm}$ ) with  $l = 2$  is the charge (spin) density operator for  $d$  electrons on site  $i$  and orbital  $m$ . The operator  $\mathbf{s}_{iL}$  is defined as  $\mathbf{s}_{iL} = \sum_{\gamma\gamma'} a_{iL\gamma}^\dagger(\boldsymbol{\sigma})_{\gamma\gamma'} a_{iL\gamma'}/2$ ,  $\boldsymbol{\sigma}$  being the Pauli spin matrices.

In the first-principles MLA, we split the Hamiltonian  $H$  into the Hartree-Fock part  $H_0$  and the residual interaction part  $H_1$ :

$$H = H_0 + H_1. \quad (2)$$

The latter is expressed as follows.

$$H_1 = \sum_i \left[ \sum_L U_{LL}^{(0)} O_{iLL}^{(0)} + \sum_{(L,L')} U_{LL'}^{(1)} O_{iLL'}^{(1)} + \sum_{(L,L')} U_{LL'}^{(2)} O_{iLL'}^{(2)} \right]. \quad (3)$$

The first term is the intra-orbital Coulomb interactions, the second term is the inter-orbital charge-charge interactions, and the third term denotes the inter-orbital spin-spin interactions,

respectively. The Coulomb interaction energy parameters  $U_{LL'}^{(\alpha)}$  are defined by  $U_{LL}\delta_{LL'}$  ( $\alpha = 0$ ),  $U_{LL'} - J_{LL'}/2$  ( $\alpha = 1$ ), and  $-2J_{LL'}$  ( $\alpha = 2$ ), respectively. The operators  $O_{iLL'}^{(0)}$ ,  $O_{iLL'}^{(1)}$ , and  $O_{iLL'}^{(2)}$  are defined by

$$O_{iLL'}^{(\alpha)} = \begin{cases} \delta n_{ilm\uparrow} \delta n_{ilm\downarrow} \delta_{LL'} & (\alpha = 0) \\ \delta n_{ilm} \delta n_{ilm'} & (\alpha = 1) \\ \delta \mathbf{s}_{ilm} \cdot \delta \mathbf{s}_{ilm'} & (\alpha = 2). \end{cases} \quad (4)$$

Note that  $\delta A$  for an operator  $A$  is defined by  $\delta A = A - \langle A \rangle_0$ ,  $\langle \sim \rangle_0$  being the average in the Hartree-Fock approximation.

When the Hamiltonian  $H$  is applied to the Hartree-Fock wavefunction  $|\phi\rangle$ , the Hilbert space is expanded by the local operators  $\{O_{iLL'}^{(\alpha)}\}$  in the interactions. In order to take into account these states as well as the states produced in the weak Coulomb interaction limit, we introduce the momentum-dependent local correlators  $\{\tilde{O}_{iLL'}^{(\alpha)}\}$  ( $\alpha = 0, 1$ , and  $2$ ) as follows.

$$\begin{aligned} \tilde{O}_{iLL'}^{(\alpha)} = \sum_{\{kn\sigma\}} & \langle k'_2 n'_2 | iL \rangle_{\sigma'_2} \langle iL | k_2 n_2 \rangle_{\sigma_2} \langle k'_1 n'_1 | iL' \rangle_{\sigma'_1} \langle iL' | k_1 n_1 \rangle_{\sigma_1} \\ & \times \lambda_{LL'\{2'21'1\}}^{(\alpha)} \delta(a_{k'_2 n'_2 \sigma'_2}^\dagger a_{k_2 n_2 \sigma_2}) \delta(a_{k'_1 n'_1 \sigma'_1}^\dagger a_{k_1 n_1 \sigma_1}). \end{aligned} \quad (5)$$

Here  $a_{kn\sigma}^\dagger$  ( $a_{kn\sigma}$ ) is the creation (annihilation) operator for an electron with momentum  $\mathbf{k}$ , band index  $n$ , and spin  $\sigma$ . These operators are given by those in the site representation as  $a_{kn\sigma} = \sum_{iL} a_{iL\sigma} \langle kn | iL \rangle_\sigma$ .  $\langle kn | iL \rangle_\sigma$  are the overlap integrals between the Bloch state ( $\mathbf{kn}$ ) and the local-orbital state ( $iL$ ).

The momentum-dependent parameters  $\lambda_{LL'\{2'21'1\}}^{(\alpha)}$  in Eq. (5) are defined as

$$\lambda_{LL'\{2'21'1\}}^{(0)} = \eta_{L[2'21'1]} \delta_{LL'} \delta_{\sigma'_2\downarrow} \delta_{\sigma_2\downarrow} \delta_{\sigma'_1\uparrow} \delta_{\sigma_1\uparrow}, \quad (6)$$

$$\lambda_{LL'\{2'21'1\}}^{(1)} = \zeta_{LL'[2'21'1]}^{(\sigma_2\sigma_1)} \delta_{\sigma'_2\sigma_2} \delta_{\sigma'_1\sigma_1}, \quad (7)$$

$$\begin{aligned} \lambda_{LL'\{2'21'1\}}^{(2)} = \sum_{\sigma} & \xi_{LL'[2'21'1]}^{(\sigma)} \delta_{\sigma'_2-\sigma} \delta_{\sigma_2\sigma} \delta_{\sigma'_1\sigma} \delta_{\sigma_1-\sigma} \\ & + \frac{1}{2} \sigma_1 \sigma_2 \xi_{LL'[2'21'1]}^{(\sigma_2\sigma_1)} \delta_{\sigma'_2\sigma_2} \delta_{\sigma'_1\sigma_1}. \end{aligned} \quad (8)$$

Here  $\{2'21'1\}$  ( $[2'21'1]$ ) implies that  $\{2'21'1\} = k'_2 n'_2 \sigma'_2 k_2 n_2 \sigma_2 k'_1 n'_1 \sigma'_1 k_1 n_1 \sigma_1$  ( $[2'21'1] = k'_2 n'_2 k_2 n_2 k'_1 n'_1 k_1 n_1$ ).  $\eta_{L[2'21'1]}$ ,  $\zeta_{LL'[2'21'1]}^{(\sigma_2\sigma_1)}$ ,  $\xi_{LL'[2'21'1]}^{(\sigma)}$ , and  $\xi_{LL'[2'21'1]}^{(\sigma_2\sigma_1)}$  are the variational parameters. Note that  $\tilde{O}_{iLL}^{(0)}$ ,  $\tilde{O}_{iLL'}^{(1)}$ , and  $\tilde{O}_{iLL'}^{(2)}$  reduce to the local correlators,  $O_{iLL}^{(0)}$ ,  $O_{iLL'}^{(1)}$ , and  $O_{iLL'}^{(2)}$  when  $\eta_{L[2'21'1]} = \zeta_{LL'[2'21'1]}^{(\sigma_2\sigma_1)} = 1$  and  $\xi_{LL'[2'21'1]}^{(\sigma)} = \xi_{LL'[2'21'1]}^{(\sigma_2\sigma_1)} = 1/2$ , so that  $\{\tilde{O}_{iLL'}^{(\alpha)}\}$  describe the intra-orbital correlations, the inter-orbital charge-charge correlations, and the inter-orbital spin-spin correlations (*i.e.*, the Hund-rule correlations), respectively.

Using the correlators  $\{\tilde{O}_{iLL'}^{(\alpha)}\}$  and the Hartree-Fock ground-state wavefunction  $|\phi\rangle$ , we

construct the first-principles MLA wavefunction as follows.

$$|\Psi_{\text{MLA}}\rangle = \left[ \prod_i \left( 1 - \sum_L \tilde{O}_{iLL}^{(0)} - \sum_{(L,L')} \tilde{O}_{iLL'}^{(1)} - \sum_{(L,L')} \tilde{O}_{iLL'}^{(2)} \right) \right] |\phi\rangle. \quad (9)$$

We note that the MLA wavefunction reduces to the local ansatz (LA) wavefunction by Stollhoff and Fulde,<sup>36–41</sup> when the variational parameters  $\lambda_{LL'\{2'21'1\}}^{(\alpha)}$  are momentum independent. The momentum dependence of the variational parameters is taken into account in order to describe exactly the weak Coulomb interaction limit.

The ground-state energy  $\langle H \rangle$  is given by

$$\langle H \rangle = \langle H \rangle_0 + N\epsilon_c. \quad (10)$$

Here  $\langle H \rangle_0$  denotes the Hartree-Fock energy,  $N$  is the number of atoms in the system.  $\epsilon_c$  is the correlation energy per atom defined by  $N\epsilon_c \equiv \langle \tilde{H} \rangle = \langle H \rangle - \langle H \rangle_0$ . Note that  $\tilde{H} \equiv H - \langle H \rangle_0 = \tilde{H}_0 + H_I$ .  $\langle \sim \rangle$  ( $\langle \sim \rangle_0$ ) denotes the full (Hartree-Fock) average with respect to  $|\Psi_{\text{MLA}}\rangle$  ( $|\phi\rangle$ ). The correlation energy  $\epsilon_c$  is expressed in the single-site approximation (SSA) as follows.<sup>20,31</sup>

$$\epsilon_c = \frac{-\langle \tilde{O}_i^\dagger H_I \rangle_0 - \langle H_I \tilde{O}_i \rangle_0 + \langle \tilde{O}_i^\dagger \tilde{H} \tilde{O}_i \rangle_0}{1 + \langle \tilde{O}_i^\dagger \tilde{O}_i \rangle_0}. \quad (11)$$

Here  $\tilde{O}_i = \sum_\alpha \sum_{\langle L, L' \rangle} \tilde{O}_{iLL'}^{(\alpha)}$ . The sum  $\sum_{\langle L, L' \rangle}$  is defined by a single sum  $\sum_L$  when  $L'=L$ , and by a pair sum  $\sum_{(L, L')}$  when  $L' \neq L$ . Each element in Eq. (11) has been calculated with use of Wick's theorem.<sup>31</sup>

The variational parameters are determined from the stationary condition  $\delta\epsilon_c = 0$  as follows.

$$-\langle (\delta \tilde{O}_i^\dagger) H_I \rangle_0 + \langle (\delta \tilde{O}_i^\dagger) \tilde{H} \tilde{O}_i \rangle_0 - \epsilon_c \langle (\delta \tilde{O}_i^\dagger) \tilde{O}_i \rangle_0 + \text{c.c.} = 0. \quad (12)$$

Here  $\delta \tilde{O}_i^\dagger$  denotes the variation of  $\tilde{O}_i^\dagger$  with respect to  $\{\lambda_{LL'\{2'21'1\}}^{(\alpha)}\}$ .

Since it is not easy to solve Eq. (12) for arbitrary Coulomb interaction strength, we make use of the following ansatz for the variational parameters, which interpolates between the weak Coulomb interaction limit and the atomic limit.<sup>30,31</sup>

$$\lambda_{LL'\{2'21'1\}}^{(\alpha)} = \frac{U_{LL'}^{(\alpha)} \sum_\tau C_{\tau\sigma_2\sigma'_2\sigma_1\sigma'_1}^{(\alpha)} \tilde{\lambda}_{\alpha\tau LL'}^{(\sigma_2\sigma_1)}}{\epsilon_{k'_2 n'_2 \sigma'_2} - \epsilon_{k_2 n_2 \sigma_2} + \epsilon_{k'_1 n'_1 \sigma'_1} - \epsilon_{k_1 n_1 \sigma_1} - \epsilon_c}. \quad (13)$$

Here the spin-dependent coefficients  $C_{\tau\sigma_2\sigma'_2\sigma_1\sigma'_1}^{(\alpha)}$  are defined by  $\delta_{\sigma'_2\downarrow} \delta_{\sigma_2\downarrow} \delta_{\sigma'_1\uparrow} \delta_{\sigma_1\uparrow}$  ( $\alpha = 0$ ),  $\delta_{\sigma'_2\sigma_2} \delta_{\sigma'_1\sigma_1}$  ( $\alpha = 1$ ),  $-(1/4) \sigma_1 \sigma_2 \delta_{\sigma'_2\sigma_2} \delta_{\sigma'_1\sigma_1}$  ( $\alpha = 2, \tau = l$ ), and  $-(1/2) \sum_\sigma \delta_{\sigma'_2-\sigma} \delta_{\sigma_2\sigma} \delta_{\sigma'_1\sigma} \delta_{\sigma_1-\sigma}$  ( $\alpha = 2, \tau = t$ ), respectively. Note that  $l(t)$  implies the longitudinal (transverse) component. The renormalization factors  $\tilde{\lambda}_{\alpha\tau LL'}^{(\sigma\sigma')}$  in Eq. (13) are defined as  $\tilde{\eta}_{LL'} \delta_{LL'} \delta_{\sigma'\sigma}$  ( $\alpha = 0$ ),  $\tilde{\zeta}_{LL'}^{(\sigma\sigma')}$  ( $\alpha = 1$ ),  $\tilde{\xi}_{tLL'}^{(\sigma)} \delta_{\sigma'\sigma}$  ( $\alpha = 2, \tau = t$ ), and  $\tilde{\xi}_{lLL'}^{(\sigma\sigma')}$  ( $\alpha = 2, \tau = l$ ), respectively. The denominator in Eq. (13) expresses the two-particle excitation energy.  $\epsilon_{kn\sigma}$  denotes the Hartree-Fock one electron energy eigenvalue for the momentum  $\mathbf{k}$ , the band index  $n$ , and spin  $\sigma$ . Note that

when  $\tilde{\eta}_{LL} = \tilde{\zeta}_{LL'}^{(\sigma\sigma')} = 1$  and  $\tilde{\xi}_{tLL'}^{(\sigma)} = \tilde{\xi}_{LL'}^{(\sigma)} = -1$ , the MLA wavefunction (9) reduces to that of the Rayleigh-Schrödinger perturbation theory in the weak Coulomb interaction limit. The renormalization factors  $\tilde{\eta}_{LL}$ ,  $\tilde{\zeta}_{LL'}^{(\sigma\sigma')}$ ,  $\tilde{\xi}_{tLL'}^{(\sigma)}$ , and  $\tilde{\xi}_{LL'}^{(\sigma\sigma')}$  are the new variational parameters to be determined.

Substituting Eq. (13) into the elements in Eq. (12), we obtain the self-consistent equations for the variational parameters. In the paramagnetic case, the variational parameters  $\tilde{\lambda}_{\alpha\tau LL'}^{(\sigma\sigma')}$  are spin independent (*i.e.*,  $\tilde{\lambda}_{\alpha\tau LL'}$ ), and the self-consistent equations are expressed as follows.<sup>31)</sup>

$$\tilde{\lambda}_{\alpha\tau LL'} = \tilde{Q}_{LL'}^{-1} \left( \kappa_{\alpha} P_{LL'} - U_{LL'}^{(\alpha)-1} K_{\tau LL'}^{(\alpha)} \right). \quad (14)$$

Here  $\tilde{Q}_{LL'}$  has the form  $\tilde{Q}_{LL'} = Q_{LL'} - \epsilon_c S_{LL'}$ . The constant  $\kappa_{\alpha}$  is defined by 1 for  $\alpha = 0, 1$ , and  $-1$  for  $\alpha = 2$ . The second terms at the rhs of Eq. (14) originates in the matrix element  $\langle \tilde{O}_i^{\dagger} H_1 \tilde{O}_i \rangle_0$  in the numerator of the correlation energy (11). These terms are of higher order in Coulomb interactions and are given by a linear combination of  $\{\tilde{\lambda}_{\alpha\tau LL'}\}$ .  $Q_{LL'}$ ,  $S_{LL'}$ ,  $P_{LL'}$ , and  $K_{\tau LL'}^{(\alpha)}$  are expressed by the Laplace transforms of the Hartree-Fock local densities of states.<sup>31)</sup>

It should be noted that  $\tilde{Q}_{LL'}$ ,  $P_{LL'}$ , and  $K_{\tau LL'}^{(\alpha)}$  contain the correlation energy  $\epsilon_c$  and the Fermi level  $\epsilon_F$ . Moreover  $K_{\tau LL'}^{(\alpha)}$  are given by a linear combination of  $\{\tilde{\lambda}_{\alpha\tau LL'}\}$ . The correlation energy  $\epsilon_c$  is expressed by Eq. (11) with variational parameters (13). The Fermi level  $\epsilon_F$  is determined by the conduction electron number per atom  $n_e$ , which is expressed as

$$n_e = \sum_L \langle n_{iL} \rangle. \quad (15)$$

Taking the same steps as in Eq. (11), we obtain the partial electron number of orbital  $L$  on site  $i$  as follows in the SSA.

$$\langle n_{iL} \rangle = \langle n_{iL} \rangle_0 + \langle \tilde{n}_{iL} \rangle. \quad (16)$$

Here  $\langle n_{iL} \rangle_0$  denotes the Hartree-Fock electron number. The correlation correction  $\langle \tilde{n}_{iL} \rangle$  is expressed as follows.

$$\langle \tilde{n}_{iL} \rangle = \frac{\langle \tilde{O}_i^{\dagger} \tilde{n}_{iL} \tilde{O}_i \rangle_0}{1 + \langle \tilde{O}_i^{\dagger} \tilde{O}_i \rangle_0}. \quad (17)$$

Note that  $\langle \tilde{O}_i^{\dagger} \tilde{n}_{iL} \rangle_0$  and  $\langle \tilde{n}_{iL} \tilde{O}_i^{\dagger} \rangle_0$ , which correspond to the first and second terms in the numerator of the correlation energy (11), vanish according to Wick's theorem. The other elements at the rhs of Eq. (17) are also calculated by using Wick's theorem. Equations (11), (14), and (15) determine self-consistently the correlation energy  $\epsilon_c$ , the Fermi level  $\epsilon_F$ , as well as the variational parameters  $\{\tilde{\lambda}_{\alpha\tau LL'}\}$ .

The momentum distribution function (MDF) is given as follows.

$$\langle n_{kn\sigma} \rangle = f(\tilde{\epsilon}_{kn\sigma}) + \frac{N \langle \tilde{O}_i^{\dagger} \tilde{n}_{kn\sigma} \tilde{O}_i \rangle_0}{1 + \langle \tilde{O}_i^{\dagger} \tilde{O}_i \rangle_0}. \quad (18)$$

The first term at the rhs is the MDF for the Hartree-Fock independent electrons, *i.e.*, the Fermi distribution function (FDF) at zero temperature.  $\tilde{\epsilon}_{kn\sigma}$  is the Hartree-Fock one-electron energy measured from the Fermi level  $\epsilon_F$ . The second term is the correlation corrections, where  $\tilde{n}_{kn\sigma}$  is defined by  $\tilde{n}_{kn\sigma} = n_{kn\sigma} - \langle n_{kn\sigma} \rangle_0$ . The numerator has the following form.<sup>31)</sup>

$$N \langle \tilde{O}_i^\dagger \tilde{n}_{kn\sigma} \tilde{O}_i \rangle_0 = \sum_{\alpha\tau \langle L, L' \rangle} q_\tau^{(\alpha)} U_{LL'}^{(\alpha)2} \tilde{\lambda}_{\alpha\tau LL'}^2 [\hat{B}_{LL'n\sigma}(\mathbf{k}) f(-\tilde{\epsilon}_{kn\sigma}) - \hat{C}_{LL'n\sigma}(\mathbf{k}) f(\tilde{\epsilon}_{kn\sigma})]. \quad (19)$$

Here  $q_\tau^{(\alpha)}$  is a constant factor taking the value 1 for  $\alpha=0$ , 2 for  $\alpha=1$ ,  $1/8$  for  $\alpha=2$ ,  $\tau=l$ , and  $1/4$  for  $\alpha=2$ ,  $\tau=t$ , respectively.  $\hat{B}_{LL'n\sigma}(\mathbf{k})$  is a momentum-dependent particle contribution above  $\epsilon_F$  and is expressed as follows.

$$\hat{B}_{LL'n\sigma}(\mathbf{k}) = |u_{Ln\sigma}(\mathbf{k})|^2 B_{L'L\sigma}(\epsilon_{kn\sigma}) + |u_{L'n\sigma}(\mathbf{k})|^2 B_{LL'\sigma}(\epsilon_{kn\sigma}), \quad (20)$$

where  $\{u_{Ln\sigma}(\mathbf{k})\}$  are the eigenvectors for a given  $\mathbf{k}$  point. The hole contribution  $\hat{C}_{LL'n\sigma}(\mathbf{k})$  is defined by Eq. (20) in which the energy dependent terms  $B_{LL'\sigma}(\epsilon_{kn\sigma})$  have been replaced by  $C_{LL'\sigma}(\epsilon_{kn\sigma})$ . These are given by the Laplace transformation of the local density of states in the Hartree-Fock approximation.<sup>31)</sup> Note that the correlation correction to  $\langle \tilde{n}_{kn\sigma} \rangle$  depends on  $\mathbf{k}$  via both energy  $\tilde{\epsilon}_{kn\sigma}$  and eigenvector  $u_{Ln\sigma}(\mathbf{k})$ .

The quasiparticle weight  $Z_{kFn}$  characterizes the low-energy excitations in metals. It is obtained by taking the difference between  $\langle n_{kn\sigma} \rangle$  below and above the Fermi level  $\epsilon_F$ . Taking average over the Fermi surface, we obtain the average quasiparticle weight  $Z$ .

$$Z = 1 + \frac{\overline{\delta(N \langle \tilde{O}_i^\dagger \tilde{n}_{kn\sigma} \tilde{O}_i \rangle_0)_{k_F}}}{1 + \langle \tilde{O}_i^\dagger \tilde{O}_i \rangle_0}. \quad (21)$$

Here the first term at the rhs denotes the Hartree-Fock part. The second term is the correlation corrections. The upper bar in the numerator denotes the average over the Fermi surface, and  $\delta(N \langle \tilde{O}_i^\dagger \tilde{n}_{kn\sigma} \tilde{O}_i \rangle_0)_{k_F}$  means the amount of jump at the wavevector  $\mathbf{k}_F$  on the Fermi surface.

In order to clarify the role of *s*, *p*, and *d* electrons, it is convenient to define the projected MDF for orbital *L* by  $\langle n_{kL\sigma} \rangle = \sum_n \langle n_{kn\sigma} \rangle |u_{Ln\sigma}(\mathbf{k})|^2$ . Furthermore, we replace the energy  $\epsilon_{kn\sigma}$  in the expression with  $\epsilon_{kL\sigma} = \sum_n \epsilon_{kn\sigma} |u_{Ln\sigma}(\mathbf{k})|^2$ , *i.e.*, a common energy band projected onto the orbital *L*. We have then

$$\langle n_{kL\sigma} \rangle = f(\tilde{\epsilon}_{kL\sigma}) + \frac{N \langle \tilde{O}_i^\dagger \tilde{n}_{kL\sigma} \tilde{O}_i \rangle_0}{1 + \langle \tilde{O}_i^\dagger \tilde{O}_i \rangle_0}. \quad (22)$$

We can also define the partial MDF  $\langle n_{kl\sigma} \rangle$  for *l* (*= s, p, d*) electrons by

$$\langle n_{kl\sigma} \rangle = \frac{1}{2l+1} \sum_m \langle n_{kL\sigma} \rangle. \quad (23)$$

It should be noted that the projected MDF depend on the momentum  $\mathbf{k}$  only via  $\tilde{\epsilon}_{kL\sigma}$ .

We can define the quasiparticle weight  $Z_L$  for electrons with orbital symmetry *L* by the



jump of  $\langle n_{kL\sigma} \rangle$  on the Fermi surface.

$$Z_L = 1 + \frac{\overline{\delta(N\langle \tilde{O}_i^\dagger \tilde{n}_{kL\sigma} \tilde{O}_i \rangle_0)_{k_F}}}{1 + \langle \tilde{O}_i^\dagger \tilde{O}_i \rangle_0}. \quad (24)$$

Then we can verify the sum rule,

$$Z = \frac{1}{D} \sum_L Z_L = \frac{1}{D} \sum_l (2l+1) Z_l. \quad (25)$$

Here  $Z_l (= \sum_m Z_{Lm}/(2l+1))$  is the quasiparticle weight for  $l (= s, p, d)$  electrons, and  $D$  is the number of orbitals per atom ( $D = 9$  in the present case). The relation allows us to interpret  $Z_l$  as a partial quasiparticle weight for the electrons with orbital  $l$ .

### 3. Numerical Results

#### 3.1 Systematic change of momentum distribution functions

In the calculations of the momentum distribution function (MDF) for the iron-group transition metals, we adopted the same lattice constants and structures as used by Andersen *et al.*,<sup>35)</sup> and constructed the tight-binding LDA+U Hamiltonians using the Barth-Hedin exchange-correlation potential.<sup>11)</sup> Furthermore we assumed orbital-independent Coulomb and

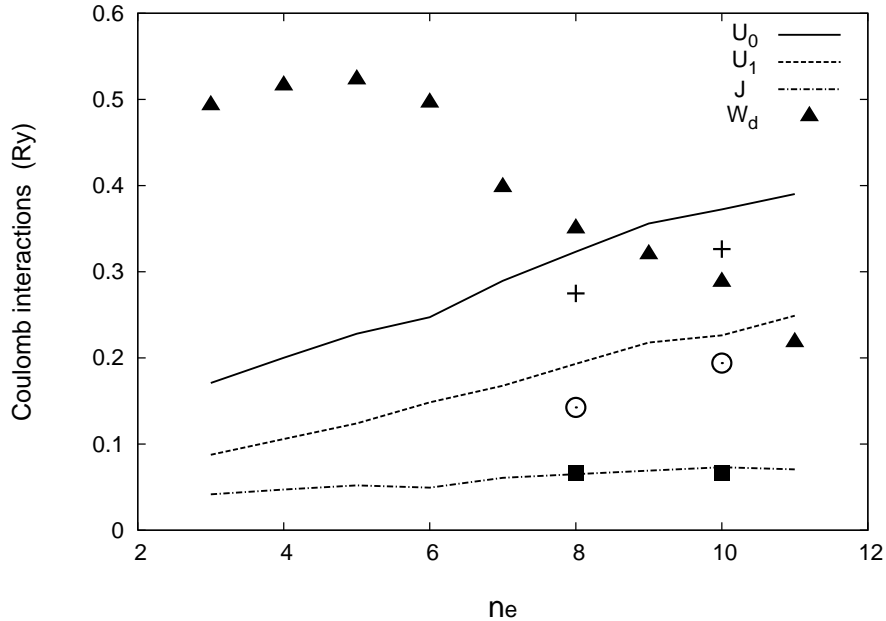


Fig. 1. Intra-atomic Coulomb and exchange energy parameters as a function of the conduction electron number  $n_e$  of iron-group transition metals. These parameters are obtained from the band<sup>42)</sup> and atomic<sup>43)</sup> calculations. Intra-orbital Coulomb interactions  $U_0$ : solid curve, inter-orbital Coulomb interactions  $U_1$ : dashed curve, exchange interactions  $J$ : dot-dashed curve.  $U_0$ ,  $U_1$ , and  $J$  used by Anisimov *et al.*<sup>44)</sup> are also shown by +,  $\odot$ , and  $\blacksquare$  for Fe ( $n_e = 8$ ) and Ni ( $n_e = 10$ ). Closed triangles  $\blacktriangle$  indicate the  $d$  band width  $W_d$ .<sup>35)</sup>

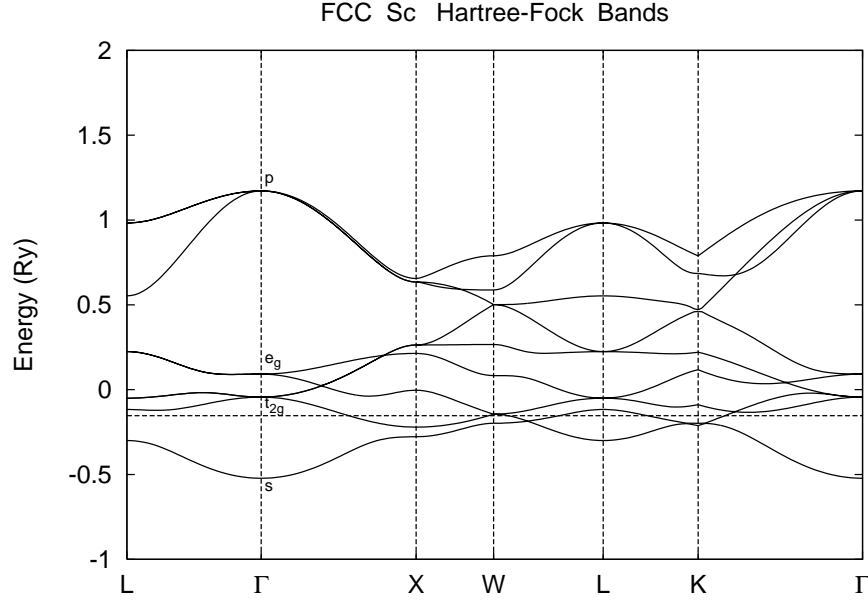


Fig. 2. Hartree-Fock one-electron energy bands of fcc Sc along high-symmetry lines of the first Brillouin zone. The Fermi level ( $-0.1538$  Ry) is expressed by the horizontal dashed line. Point symmetries of eigen functions at the  $\Gamma$  point are expressed by  $s$ ,  $p$ ,  $e_g$ , and  $t_{2g}$ .

exchange interactions  $U_{mm} = U_0$ ,  $U_{mm'} = U_1$  ( $m' \neq m$ ), and  $J_{mm'} = J$ . These values are obtained from the average Coulomb interaction energies  $U$  via the relations  $U_0 = U + 8J/5$  and  $U_1 = U - 2J/5$  for the cubic system. We applied the average interactions  $U$  obtained by Bandyopadhyay *et al.*<sup>42)</sup> and the average  $J$  obtained from the Hartree-Fock atomic calculations.<sup>43)</sup> The Coulomb and exchange interaction energies from Sc and Cu are depicted in Fig. 1 as a function of the conduction electron number  $n_e$ . The same Hamiltonian and Coulomb-exchange interactions have been applied in the investigations of the excitation spectra in 3d transition metals with use of the first-principles DCPA.<sup>24)</sup>

We performed the self-consistent Hartree-Fock calculations from Sc to Cu in the paramagnetic state using the tight-binding LDA+U Hamiltonian. With use of the Hartree-Fock energy bands and eigenvectors, we solved the self-consistent equations (11), (14), and (15), and calculated the momentum distribution functions (MDF) from Sc to Cu according to Eq. (18).

As has been discussed in the last paper,<sup>32)</sup> the  $d$  band widths in the Hartree-Fock approximation are broader than the LDA ones for the elements with  $d$  electrons less than half by about 10-30 %, while they shrink for the elements with  $d$  electrons more than half by several percent. We show the calculated Hartree-Fock energy bands of fcc Sc along high-symmetry lines in Fig. 2. There are 4 eigenvalues at point  $\Gamma$ :  $-0.522$  Ry for  $s$  electrons below the Fermi level  $\epsilon_F$  ( $= -0.154$  Ry),  $-0.044$  Ry for  $t_{2g}$  electrons above  $\epsilon_F$ ,  $0.092$  Ry for  $e_g$  electrons, and

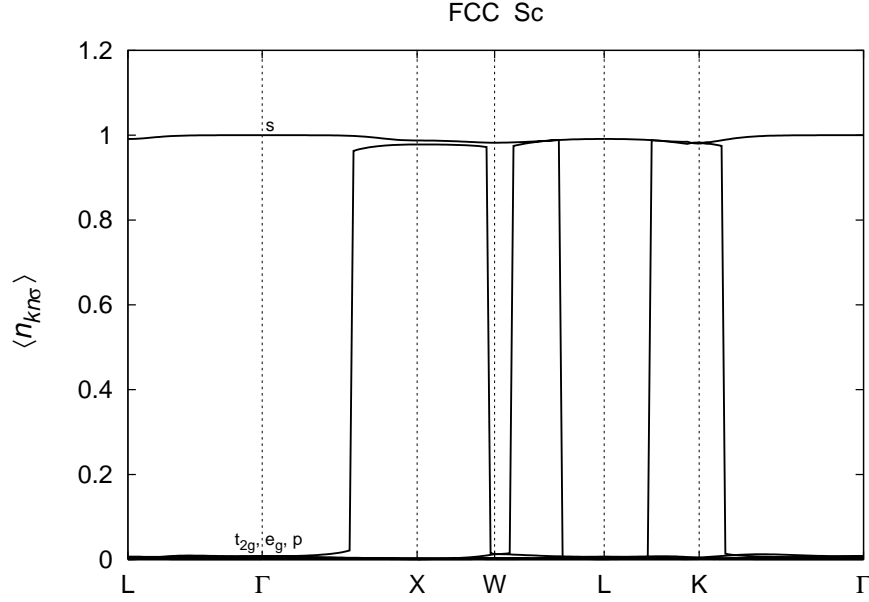


Fig. 3. Momentum distribution functions  $\langle n_{k\sigma} \rangle$  along high-symmetry lines for fcc Sc. The branches at the  $\Gamma$  point are shown by their orbital symmetries (*i.e.*,  $s$ ,  $p$ ,  $e_g$ , and  $t_{2g}$ ).

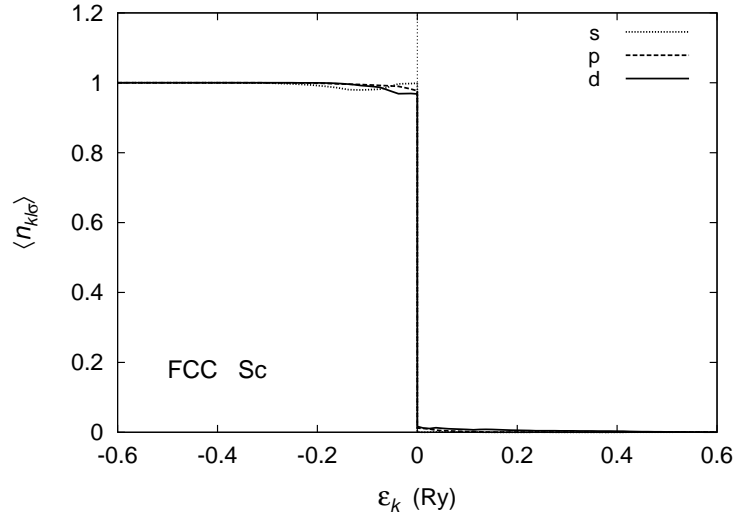


Fig. 4. The projected momentum distribution functions (MDF)  $\langle n_{kl\sigma} \rangle$  as a function of the energy  $\epsilon_k$  ( $= \epsilon_{kL\sigma} - \epsilon_F$ ) for fcc Sc. Dotted curve: the MDF for  $s$  electrons ( $l = 0$ ), dashed curve: the MDF for  $p$  electrons ( $l = 1$ ), solid curve: the MDF for  $d$  electrons ( $l = 2$ ).

1.172 Ry for  $p$  electrons. When the wavevector  $\mathbf{k}$  moves to point  $X$  along the  $\Gamma$ - $X$  line, the energy for  $s$  electrons below  $\epsilon_F$  increases, hybridizes with  $e_g$  electrons, and has a value  $-0.277$  Ry at point  $X$ . The energy band for  $t_{2g}$  electrons above  $\epsilon_F$  splits into two branches with the change of  $\mathbf{k}$  towards point  $X$ . One decreases, crosses the Fermi level at  $\mathbf{k}_F = (0, 0.58, 0)$  in the

unit of  $2\pi/a$ ,  $a$  being the lattice constant, and takes a value  $-0.220$  Ry with the  $xz$  symmetry at point X. Another is two-fold degenerate, and increases, takes a value  $0.263$  Ry at point

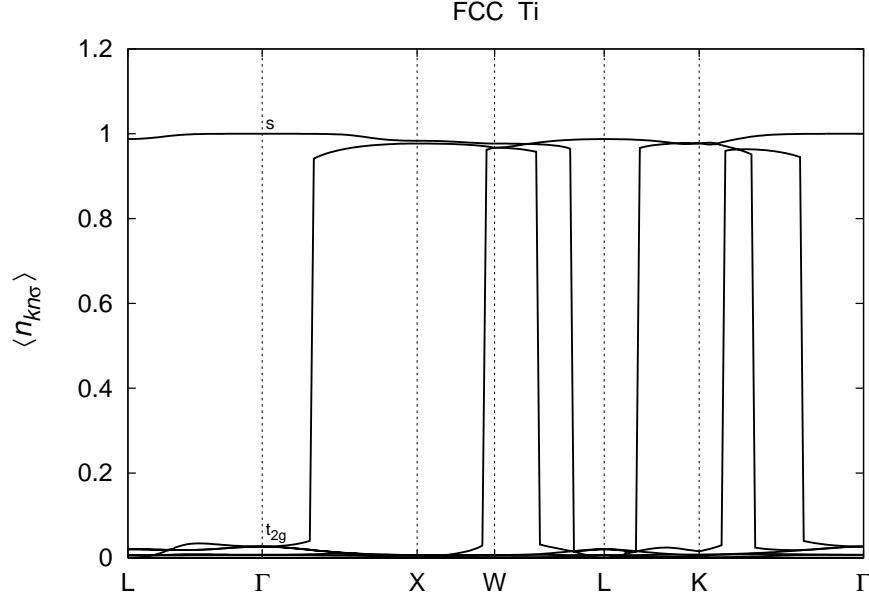


Fig. 5. Momentum distribution functions  $\langle n_{k\sigma} \rangle$  along high-symmetry lines for fcc Ti.

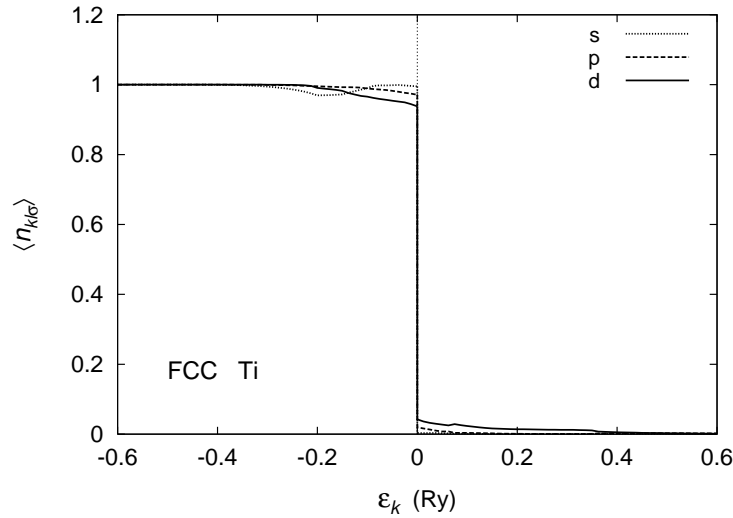


Fig. 6. The projected MDF  $\langle n_{kl\sigma} \rangle$  as a function of the energy  $\epsilon_k$  for fcc Ti. Dotted curve: the MDF for  $s$  electrons, dashed curve: the MDF for  $p$  electrons, solid curve: the MDF for  $d$  electrons.

X. The energy band for  $e_g$  electrons splits into two branches on the  $\Gamma$ -X line. One decreases

with the change of  $\mathbf{k}$  towards point X, and takes a value  $-0.004$  Ry with  $y$  symmetry at point X. Another gradually increases with the change of  $\mathbf{k}$ , and takes a value  $0.213$  Ry with  $e_g$  symmetry at point X. Note that the MDF in the Hartree-Fock approximation takes the value 1 for occupied electrons below  $\epsilon_F$  and the value 0 for unoccupied electrons above  $\epsilon_F$ , and jumps at the Fermi surface by  $\pm 1$ .

We present in Fig. 3 the MDF for fcc Sc. The MDF for  $s$  electrons with energy below  $\epsilon_F$  has a value 1.000 at point  $\Gamma$  in agreement with the result of the Fermi distribution function (FDF), *i.e.*,  $f(\tilde{\epsilon}_{kn\sigma})$ . It slightly decreases when the wavevector  $\mathbf{k}$  moves to point X along the  $\Gamma$ -X line, and takes a value 0.988 at point X, which is slightly smaller than the Hartree-Fock value 1, because of the electron correlations of  $e_g$  electrons via hybridization between the  $s$  and  $e_g$  electrons. The MDF for  $t_{2g}$  electrons with  $xz$  symmetry above  $\epsilon_F$  shows a small value 0.007 at point  $\Gamma$  and increases with the change of  $\mathbf{k}$  towards point X, jumps up from 0.021 to 0.963 at  $\mathbf{k}_F = (0, 0.58, 0)$ , and increases further. The quasiparticle weight at  $\mathbf{k}_F = (0, 0.58, 0)$  has a value  $Z_{kn} = 0.942$ , thus the mass enhancement factor  $m_{kn}^*/m = 1.062$ . The MDF has a value 0.978 at point X. The MDF for the other  $t_{2g}$  electrons decreases from 0.007 to 0.000 with the change of  $\mathbf{k}$  on the  $\Gamma$ -X line. The MDF for  $e_g$  and  $p$  electrons with energy above  $\epsilon_F$  have the value 0.000 in agreement with the result of the Hartree-Fock FDF. Similar behavior is found also in the MDF along the X-W-L-K- $\Gamma$  lines.

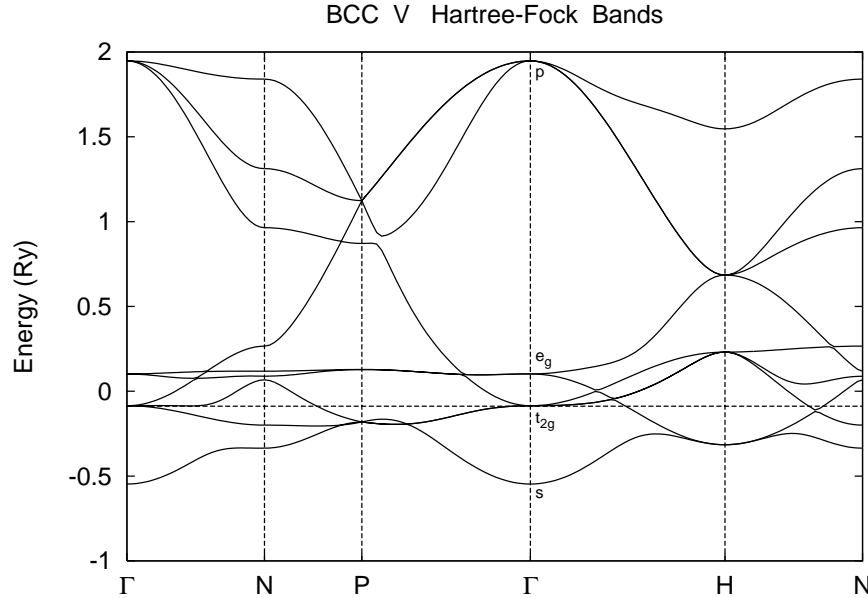


Fig. 7. Hartree-Fock one-electron energy bands of bcc V along high-symmetry lines. The Fermi level ( $-0.0884$  Ry) is expressed by the horizontal dashed line.

In order to make clearer the role of the  $s$ ,  $p$ , and  $d$  electrons, we calculated the projected

MDF for Sc as shown in Fig. 4. We verify that the MDF for  $s$ ,  $p$ , and  $d$  electrons approximately follow the FDF in the case of Sc, and thus behave as the independent electrons, though the MDF for  $d$  electrons show a small deviation from the FDF near the Fermi levels ( $\epsilon_k = 0$ ).

The band structure of fcc Ti is basically the same as the fcc Sc. The Fermi level relatively shifts up and the  $d$  bands are filled more because of larger conduction electron number  $n_e$ . Accordingly, the deviation of the MDF from the FDF becomes larger in fcc Ti as shown in Fig. 5. The MDF for  $t_{2g}$  electrons has a larger value 0.027 at point  $\Gamma$ , and jumps up at  $\mathbf{k}_F = (0, 0.33, 0)$  when the wavevector  $\mathbf{k}$  moves to point X. The quasiparticle weight obtained there has smaller value  $Z_{kn} = 0.901$  as compared with the value  $Z_{kn} = 0.942$  in Sc, thus larger mass enhancement  $m_{kn}/m = 1.109$ . Another branch of  $t_{2g}$  electrons decreases with the change of  $\mathbf{k}$  towards point X, and has a value 0.007 at point X. The MDF curve for  $t_{2g}$  electrons on the  $\Gamma$ -L line shows a broad peak around  $\mathbf{k} = (0.26, 0.26, 0.26)$  because the corresponding  $\epsilon_{kn}$  shows the minimum there. The  $s$  electrons with energy below  $\epsilon_F$  and  $p$  electrons above  $\epsilon_F$  behave as the independent electrons as in the case of Sc.

Figure 6 shows the projected MDF for fcc Ti. The MDF for  $s$  electrons show a small dip around  $\epsilon_k = -0.2$  Ry due to electron correlations via the  $sd$  hybridization. The MDF for  $p$  electrons also shows a small momentum dependence for the same reason. The MDF for  $d$  electrons shows larger momentum dependence. Calculated partial mass enhancement factors are  $m_s^*/m = 1.008$ ,  $m_p^*/m = 1.051$ , and  $m_d^*/m = 1.117$ , respectively.

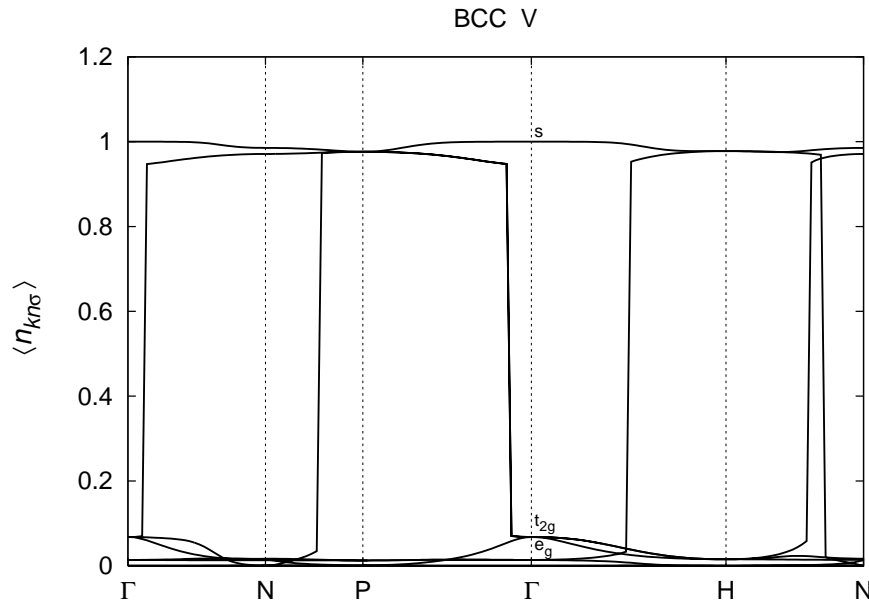


Fig. 8. Momentum distribution functions  $\langle n_{kn\sigma} \rangle$  along high-symmetry lines for bcc V.

The Hartree-Fock band structure for bcc V is presented in Fig. 7. The energy eigenvalues

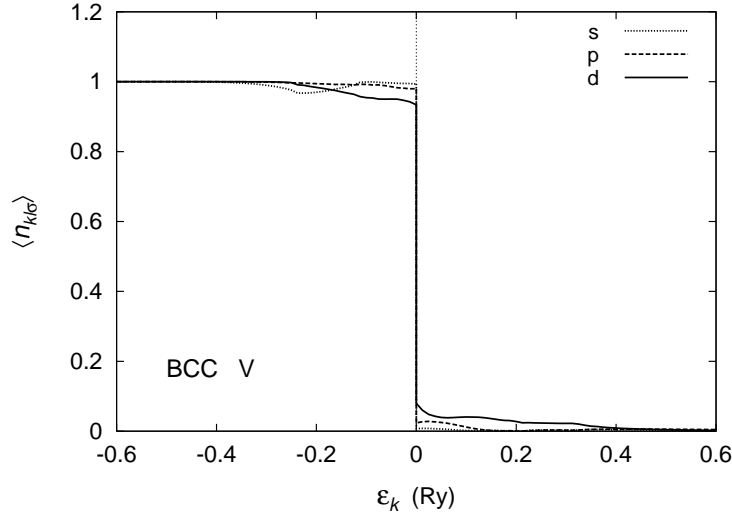


Fig. 9. The projected MDF  $\langle n_{kl\sigma} \rangle$  as a function of the energy  $\epsilon_k$  for bcc V. Dotted curve: the MDF for  $s$  electrons, dashed curve: the MDF for  $p$  electrons, solid curve: the MDF for  $d$  electrons.

at point  $\Gamma$  are  $-0.547$  Ry for  $s$  electrons below  $\epsilon_F$ ,  $-0.085$  Ry for  $t_{2g}$  electrons just above  $\epsilon_F (= -0.088$  Ry),  $0.102$  Ry for  $e_g$  electrons above  $\epsilon_F$ , and  $1.948$  Ry for  $p$  electrons far above  $\epsilon_F$ . When the wavevector  $\mathbf{k}$  moves to point H along the  $\Gamma$ -H line, the energy bands for  $e_g$  and  $t_{2g}$  electrons split into two branches respectively. Among them, one of the branches for  $e_g$  electrons crosses the Fermi level at  $\mathbf{k}_F = (0, 0.49, 0)$ , where the Hartree-Fock MDF changes the value from 0 to 1 according to the FDF.

The MDF curves of bcc V for correlated electrons are presented in Fig. 8. There are 4 different MDF at point  $\Gamma$  whose values are 1.000 for  $s$  electrons with energy below  $\epsilon_F$ , 0.068 for  $t_{2g}$  electrons just above  $\epsilon_F$ , 0.014 for  $e_g$  electrons above  $\epsilon_F$ , and 0.000 for  $p$  electrons, respectively. When the wavevector  $\mathbf{k}$  moves to point H along the  $\Gamma$ -H line, the MDF for  $s$  electrons slightly decreases due to the  $sd$  hybridization and has a value 0.977 at point H. The MDF for  $t_{2g}$  electrons splits into two branches. Both branches gradually decrease with the change of  $\mathbf{k}$  towards point H and again merge into a single band with the value 0.015 at point H. The MDF for  $e_g$  electrons also splits into two branches. One monotonically decreases and reduces to zero at point H. Another branch monotonically increases with the change of  $\mathbf{k}$ , jumps up at  $\mathbf{k}_F = (0, 0.50, 0)$  from 0.033 to 0.953, and has a value 0.977 at point H. The MDF for  $p$  electrons are almost zero on the  $\Gamma$ -H line because the corresponding energies  $\epsilon_{kn}$  are far above  $\epsilon_F$ . The jumps at  $\mathbf{k}_F = (0.50, 0.50, 0.09)$  along the  $\Gamma$ -N line and  $\mathbf{k}_F = (0.07, 0.07, 0.07)$  along the P- $\Gamma$  line yield the smallest quasiparticle weight  $Z_{kn}$ , thus the largest mass enhancement factor  $m_{kn}^*/m = 1.140$  which is larger than that of the fcc Ti.

In Fig. 9, we show the projected MDF for bcc V. We find that the basic behavior is similar to that in the fcc Ti (see Fig. 6). However the deviation of the MDF for  $d$  electrons from the

FDF becomes larger.

The Hartree-Fock band structure of bcc Cr is similar to the bcc V. The Fermi level is shifted up by about 0.06 Ry, so that new Fermi surfaces appear at  $\mathbf{k}_F = (0.20, 0.20, 0)$  on the  $\Gamma$ -N line,  $\mathbf{k}_F = (0, 0.37, 0)$  and  $(0, 0.60, 0)$  on the  $\Gamma$ -H line. Accordingly new jumps of the MDF

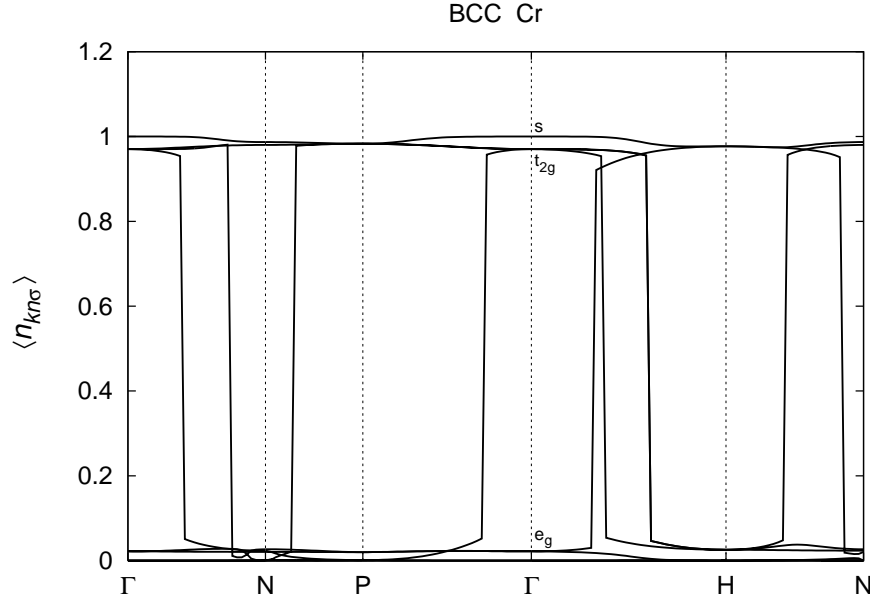


Fig. 10. Momentum distribution functions  $\langle n_{k\sigma} \rangle$  along high-symmetry lines for bcc Cr.

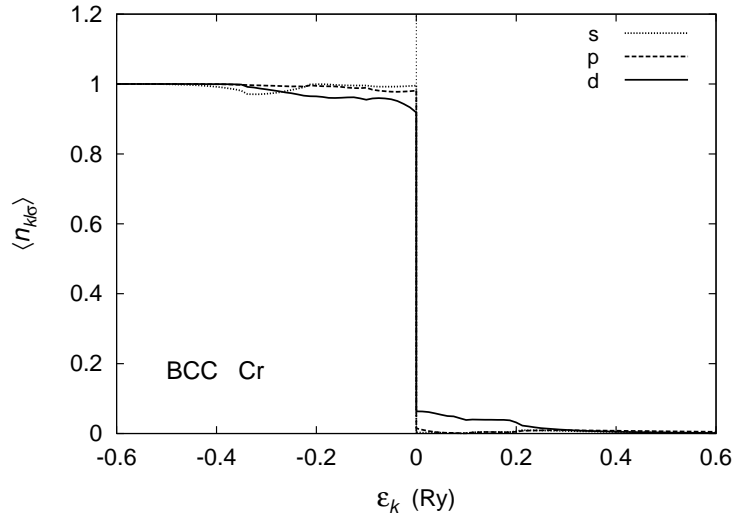


Fig. 11. The projected MDF  $\langle n_{kl\sigma} \rangle$  as a function of the energy  $\epsilon_k$  for bcc Cr. Dotted curve: the MDF for  $s$  electrons, dashed curve: the MDF for  $p$  electrons, solid curve: the MDF for  $d$  electrons.



appear at these  $\mathbf{k}$  points as shown in Fig. 10. The deviations of the MDF from the FDF are comparable to those in the bcc V. Calculated projected MDF also show the behavior similar to the bcc V as shown in Fig. 11, though the dip of the MDF for  $s$  electrons due to the  $sd$  hybridization is now located around  $\epsilon_k = -0.3$  Ry.

Next, we discuss the MDF for fcc Mn. The fcc Mn has larger Coulomb and exchange interactions as shown in Fig. 1. The band structure is shown in Fig. 12. The  $e_g$  bands sink more with increasing the electron number  $n_e$ , and are located on the Fermi level. Because the  $e_g$  bands are narrow and the  $t_{2g}$  bands are also located near the Fermi level, calculated MDF for  $d$  electrons are expected to show a large deviation from the FDF.

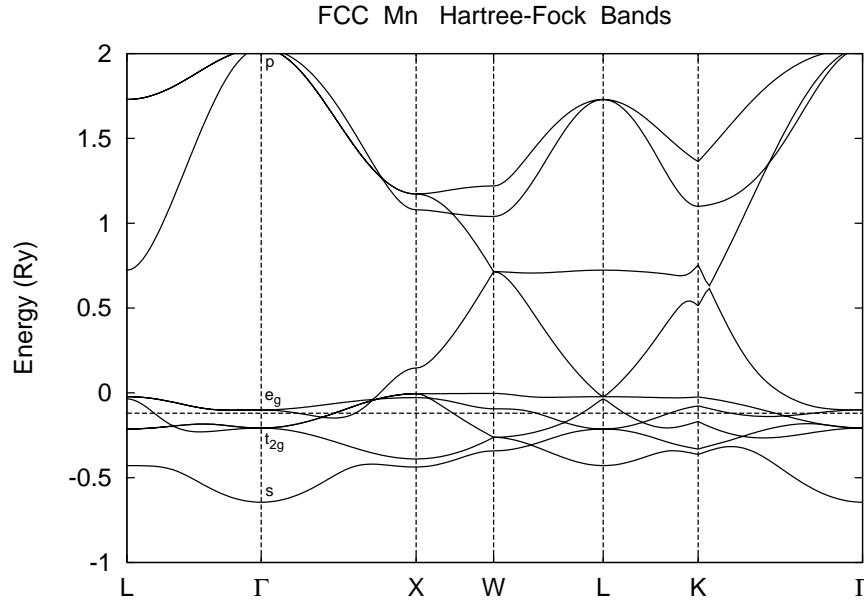


Fig. 12. Hartree-Fock one-electron energy bands of fcc Mn along high-symmetry lines. The Fermi level ( $-0.1201$  Ry) is expressed by the horizontal dashed line.

Figure 13 shows the MDF for fcc Mn along high-symmetry lines. The MDF for  $s$  band has a value 1.000 at point  $\Gamma$ . When the wavevector  $\mathbf{k}$  moves to point X along the  $\Gamma$ -X line, it monotonically decreases due to hybridization between  $s$  and  $t_{2g}$  electrons, and has a value 0.970 at point X. The MDF for  $d$  electrons show distinct deviation from the FDF. The MDF for  $t_{2g}$  electrons with energy below  $\epsilon_F$  has a value 0.954 at point  $\Gamma$ . With the change of  $\mathbf{k}$  towards point X it splits into two branches. The upper branch with  $xy$  symmetry slightly increases and has a value 0.977 at point X. The lower branch decreases along the  $\Gamma$ -X line, jumps down at  $\mathbf{k}_F = (0, 0.47, 0)$ , and reaches the X point. It has a value 0.060 at point X. The MDF for  $e_g$  electrons has a value 0.112 at point  $\Gamma$ . It splits into two branches along the  $\Gamma$ -X line. The first branch monotonically decreases with the change of  $\mathbf{k}$  and takes a value

0.074 at point X. The second one increases first, jumps up at  $\mathbf{k}_F = (0, 0.22, 0)$ , and increases further along the  $\Gamma$ -X line. But it again jumps down at  $\mathbf{k}_F = (0, 0.59, 0)$ . Finally it decreases and has the value 0.000 with the  $p$  symmetry at point X. The MDF for  $e_g$  electrons show

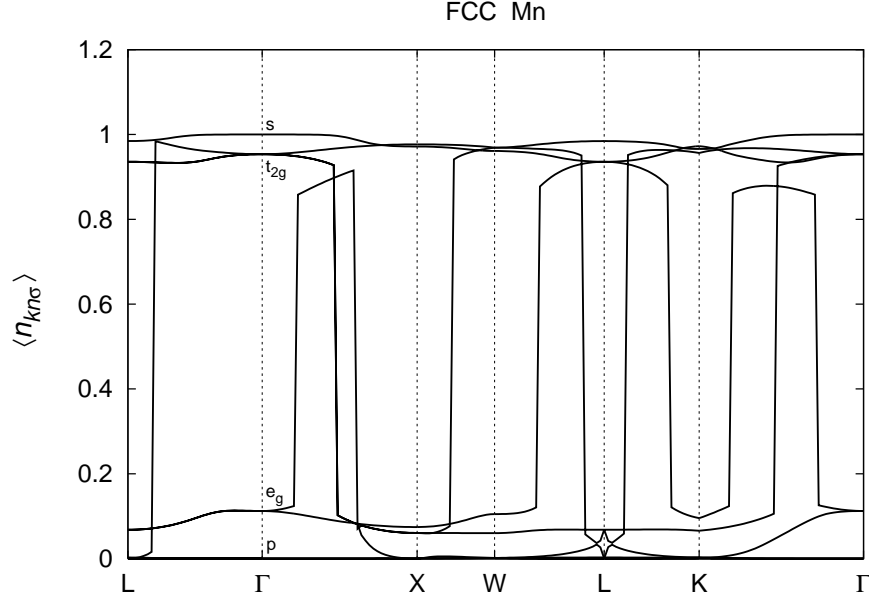


Fig. 13. Momentum distribution functions  $\langle n_{k\sigma} \rangle$  along high-symmetry lines for fcc Mn.

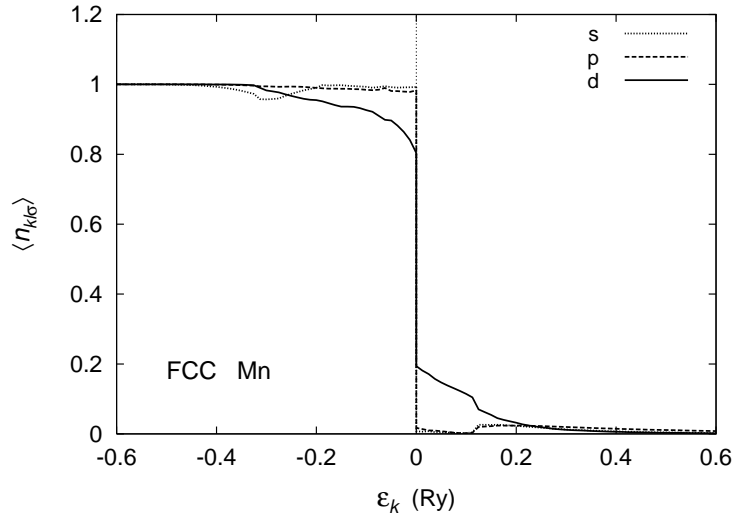


Fig. 14. The projected MDF  $\langle n_{kl\sigma} \rangle$  as a function of the energy  $\epsilon_k$  for fcc Mn. Dotted curve: the MDF for  $s$  electrons, dashed curve: the MDF for  $p$  electrons, solid curve: the MDF for  $d$  electrons.

more significant deviations from the FDF than those for  $t_{2g}$  case, and show a considerable

mass enhancement on the Fermi surface:  $m_{kn}^*/m = 1.362$  at  $\mathbf{k}_F = (0, 0.22, 0)$  on the  $\Gamma$ -X line and  $m_{kn}^*/m = 1.365$  at  $\mathbf{k}_F = (0, 0.21, 0.21)$  on the K- $\Gamma$  line.

The projected MDF for fcc Mn show a clear difference between the  $d$  electrons and  $sp$  electrons as seen in Fig. 14. The MDF for  $d$  electrons shows a strong momentum dependence due to electron correlations, while those for  $sp$  electrons are rather close to the FDF. We find the partial mass enhancement factors,  $m_s^*/m = 1.015$ ,  $m_p^*/m = 1.035$ , and  $m_d^*/m = 1.640$ , respectively.

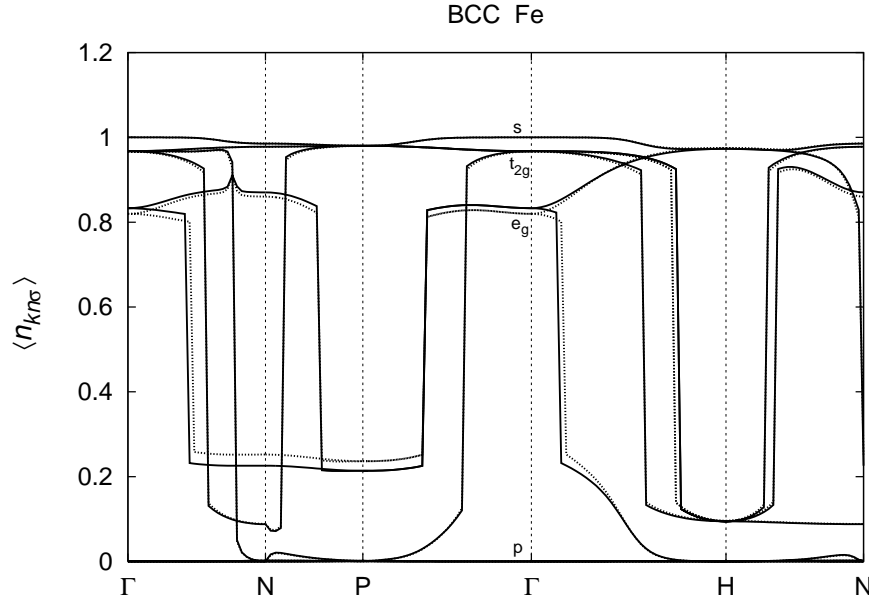


Fig. 15. Momentum distribution functions  $\langle n_{kn\sigma} \rangle$  along high symmetry lines for bcc Fe. Dotted curves are the result<sup>30)</sup> with use of  $U = 0.1691$  Ry and  $J = 0.0662$  Ry.<sup>44)</sup>

We have discussed the MDF for bcc Fe with use of the average Coulomb and exchange interactions  $U = 0.1691$  Ry and  $J = 0.0662$  Ry<sup>44)</sup> recently.<sup>30)</sup> We present here the results for  $U = 0.2192$  Ry and  $J = 0.0650$  Ry obtained by Bandyopadhyay *et al.* and the Hartree-Fock atomic calculations as mentioned before. Figure 15 shows the MDF for Fe along high-symmetry lines. As seen from the figure, the difference in the MDF between two sets of  $U$  and  $J$  is small. At point  $\Gamma$ , we have 4 branches of the MDF. The MDF for  $s$  electrons with energy eigen value  $-0.687$  Ry below  $\epsilon_F$  ( $= -0.134$  Ry) has a value 1.000 at point  $\Gamma$ . It monotonically decreases when the wavevector  $\mathbf{k}$  moves to point H along the  $\Gamma$ -H line, and takes a value 0.973 at point H.

The MDF for  $t_{2g}$  electrons with energy  $-0.263$  Ry below  $\epsilon_F$  has a value 0.967 at point  $\Gamma$ . With the change of  $\mathbf{k}$  towards point H, it splits into two branches. The first branch decreases with the change of  $\mathbf{k}$ , jumps down at  $\mathbf{k}_F = (0, 0.76, 0)$ , and finally takes a value 0.095 at point

H. Another branch decreases more rapidly, jumps down at  $\mathbf{k}_F = (0, 0.58, 0)$  and has the same value 0.095 at point H.

The MDF for  $e_g$  electrons with energy just below  $\epsilon_F$  shows the largest deviation from the FDF (=1), *i.e.*,  $\langle n_{kn\sigma} \rangle = 0.832$  at point  $\Gamma$  because the flat bands of  $e_g$  electrons along  $\Gamma$ -N-P- $\Gamma$  line are located on the Fermi level in the case of bcc Fe (see Fig. 7). It splits into two branches with the change of  $\mathbf{k}$  towards point H. The first branch monotonically increases and takes a value 0.973 at point H. The second branch decreases, and jumps down at  $\mathbf{k}_F = (0, 0.14, 0)$  from 0.823 to 0.232. It further decreases with the change of the symmetry from the  $e_g$  to  $sp$  type, and takes the value 0.000 at point H. We find that the  $e_g$  electrons cause a large deviation of the MDF from the FDF because of the strong electron correlations in the narrow  $e_g$  band on the Fermi level.

Table I. Mass enhancement factors of bcc Fe for  $e_g$  electrons at various wave vectors  $\mathbf{k}$  on the Fermi surface.

| $\mathbf{k}$ | (0.22, 0.22, 0.00) | (0.50, 0.50, 0.28) | (0.32, 0.32, 0.32) | (0.00, 0.14, 0.00) |
|--------------|--------------------|--------------------|--------------------|--------------------|
| $m_{kn}^*/m$ | 1.70               | 1.61               | 1.66               | 1.69               |

Table II. Mass enhancement factors of bcc Fe for  $t_{2g}$  electrons at various wave vectors  $\mathbf{k}$  on the Fermi surface.

| $\mathbf{k}$ | (0.28, 0.28, 0.00) | (0.39, 0.39, 0.00) | (0.50, 0.50, 0.09) | (0.29, 0.29, 0.29) |
|--------------|--------------------|--------------------|--------------------|--------------------|
| $m_{kn}^*/m$ | 1.26               | 1.12               | 1.14               | 1.23               |

| $\mathbf{k}$ | (0.00, 0.58, 0.00) | (0.00, 0.76, 0.00) | (0.15, 0.85, 0.00) | (0.18, 0.82, 0.00) |
|--------------|--------------------|--------------------|--------------------|--------------------|
| $m_{kn}^*/m$ | 1.27               | 1.25               | 1.23               | 1.26               |

The projected MDF for  $d$  electrons shows the strong momentum dependence especially near the Fermi level as shown in Fig. 16. From the jumps of the projected MDF at  $\epsilon_F$ , we find the partial mass enhancement factors:  $m_s^*/m = 1.007$ ,  $m_p^*/m = 1.010$ , and  $m_d^*/m = 2.720$ , respectively. Considerable deviations of the projected MDF from the FDF are also found for  $s$  and  $p$  electrons. They are caused by the hybridization between  $sp$  and  $d$  electrons.

We also calculated the MDF for fcc Fe to clarify the difference in the MDF between the bcc and fcc structures. The fcc Fe shows the band structure similar to the fcc Mn (see Fig. 12). Because of the change of the Fermi level, the  $e_g$  bands of fcc Fe measured from  $\epsilon_F$  sink

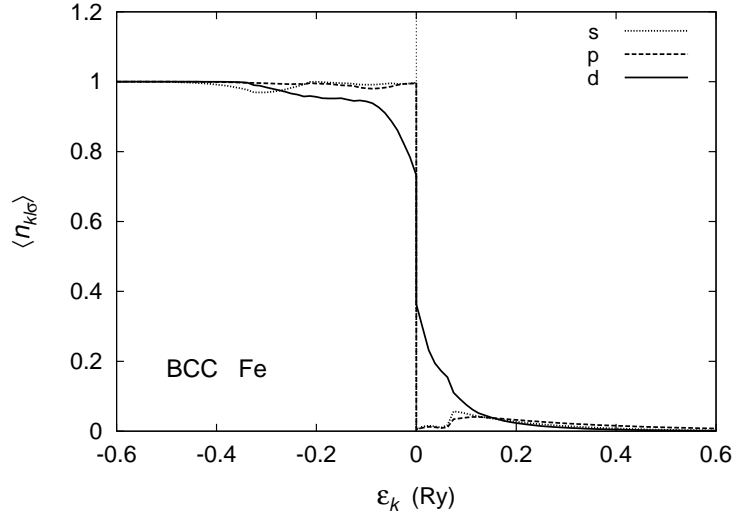


Fig. 16. The projected MDF  $\langle n_{kl\sigma} \rangle$  as a function of the energy  $\epsilon_k$  for bcc Fe. Dotted curve: the MDF for  $s$  electrons, dashed curve: the MDF for  $p$  electrons, solid curve: the MDF for  $d$  electrons.

and are located just below  $\epsilon_F$  at points  $\Gamma$  and  $W$ , and just above  $\epsilon_F$  at point  $K$ . Accordingly, the MDF for  $e_g$  electrons at point  $\Gamma$ ,  $W$ ,  $K$  shift up to 0.916, 0.913, and 0.185, respectively as shown in Fig. 17, when they are compared with those in fcc Mn (see Fig. 13). The MDF for  $t_{2g}$  electrons with energy above  $\epsilon_F$  (*e.g.*,  $\langle n_{kn\sigma} \rangle = 0.956$  at point  $\Gamma$ ) is somewhat shifted up in comparison with those for fcc Mn because their band energies measured from  $\epsilon_F$  sink more. The other MDF bands shows the behavior similar to those for the fcc Mn.

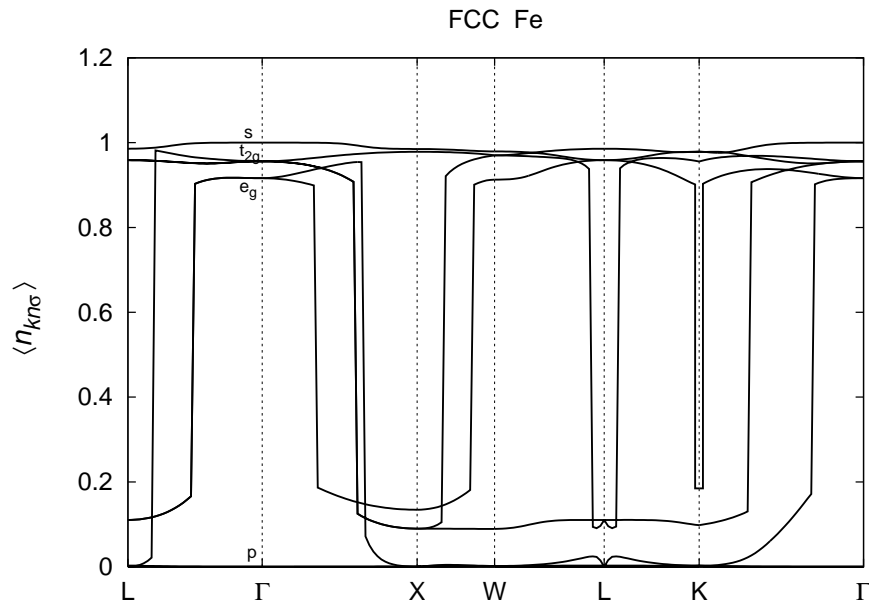


Fig. 17. Momentum distribution functions  $\langle n_{kn\sigma} \rangle$  along high-symmetry lines for fcc Fe.

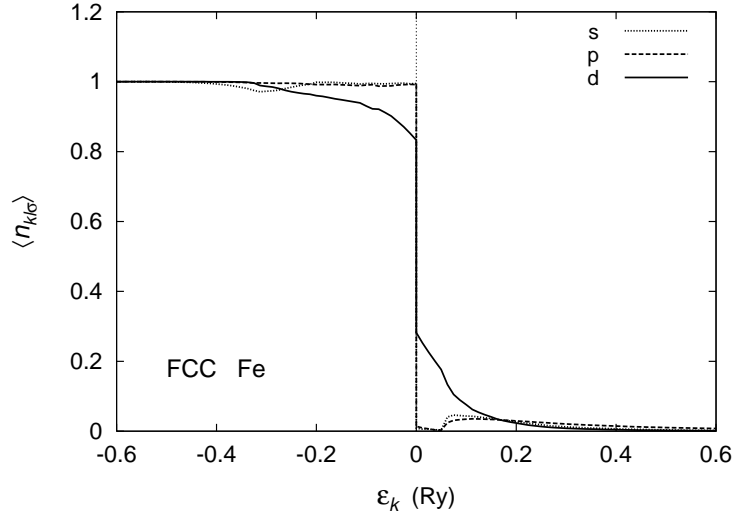


Fig. 18. The partial MDF  $\langle n_{kl\sigma} \rangle$  as a function of the energy  $\epsilon_k$  for fcc Fe. Dotted curve: the MDF for  $s$  electrons, dashed curve: the MDF for  $p$  electrons, solid curve: the MDF for  $d$  electrons.

Table III. Mass enhancement factors of fcc Fe for  $e_g$  electrons at various wave vectors  $\mathbf{k}$  on the Fermi surface.

| $\mathbf{k}$ | (0.24, 0.24, 0.24) | (0.00, 0.35, 0.00) | (0.00, 0.65, 0.00) | (0.36, 1.00, 0.00) |
|--------------|--------------------|--------------------|--------------------|--------------------|
| $m_{kn}^*/m$ | 1.36               | 1.40               | 1.13               | 1.39               |

| $\mathbf{k}$ | (0.01, 0.74, 0.74) | (0.00, 0.74, 0.74) | (0.00, 0.23, 0.23) |
|--------------|--------------------|--------------------|--------------------|
| $m_{kn}^*/m$ | 1.40               | 1.39               | 1.37               |

We compare the mass enhancement factors of fcc Fe along high-symmetry lines with those of the bcc Fe in Tables I, II, III, IV. Although the MDF for  $e_g$  electrons in both the fcc and bcc Fe show a significant deviation from the FDF, the bcc Fe shows larger mass enhancement on the Fermi surface. This is because the  $e_g$  electrons for the bcc Fe are more localized and form a flat energy dispersion on the Fermi surface. The mass enhancement factors for  $t_{2g}$  electrons approximately lead to the same average values  $m_{t_{2g}}^*/m \approx 1.2$  for both structures, but those of the fcc Fe show stronger momentum dependence.

In Fig. 18, we present the projected MDF for fcc Fe. Calculated mass enhancement factors for  $s$ ,  $p$ , and  $d$  electrons are  $m_s^*/m = 1.014$ ,  $m_p^*/m = 1.023$ , and  $m_d^*/m = 1.815$ , respectively. We find that the  $s$ ,  $p$ , and  $d$  projected MDF curves of fcc Fe show the similar behavior as the bcc ones. But in the low energy region  $|\epsilon_k| \lesssim 0.05$  Ry, the  $d$  projected MDF of the bcc Fe shows stronger momentum dependence leading to larger effective mass enhancement.

The band structure of the fcc Co is similar to those of the fcc Mn and fcc Fe (see Fig. 12).

Table IV. Mass enhancement factors of fcc Fe for  $t_{2g}$  electrons at various wave vectors  $\mathbf{k}$  on the Fermi surface.

| $\mathbf{k}$ | (0.40, 0.40, 0.40) | (0.00, 0.60, 0.00) | (0.17, 1.00, 0.00) |
|--------------|--------------------|--------------------|--------------------|
| $m_{kn}^*/m$ | 1.04               | 1.28               | 1.23               |

| $\mathbf{k}$ | (0.50, 0.56, 0.44) | (0.43, 0.54, 0.54) | (0.00, 0.52, 0.52) |
|--------------|--------------------|--------------------|--------------------|
| $m_{kn}^*/m$ | 1.19               | 1.18               | 1.29               |

However, the  $e_g$  bands sink more below  $\epsilon_F$ , and the  $t_{2g}$  flat bands above  $\epsilon_F$  along the X-W-L-K line approach to  $\epsilon_F$ . Thus the MDF for  $e_g$  electrons below  $\epsilon_F$  become closer to one as shown in Fig. 19, and the MDF for  $t_{2g}$  electrons become larger. In fact, the MDF for  $e_g$  electrons at point  $\Gamma$  moves from 0.916 to 0.970 when fcc Fe changes to fcc Co (see Figs. 17 and 19), and the MDF for  $t_{2g}$  electrons at point  $\Gamma$  moves from 0.956 to 0.979 for the same change. The flat MDF band for  $t_{2g}$  electrons along the X-W-L-K line has slightly enhanced value ( $\approx 0.13$ ). Calculated projected MDF for fcc Co are shown in Fig. 20. The projected MDF are similar to those in the fcc Fe, but the momentum dependence for  $d$  electrons becomes weaker.

In the case of fcc Ni, the  $d$  bands measured from the Fermi level  $\epsilon_F$  sink further as shown in Fig. 21. Most of the  $e_g$  bands are located below  $\epsilon_F$ . The  $t_{2g}$  branch at point  $\Gamma$  is also located below  $\epsilon_F$ . But, the flat band of  $t_{2g}$  electrons along the X-W-L-K line is on the Fermi level.

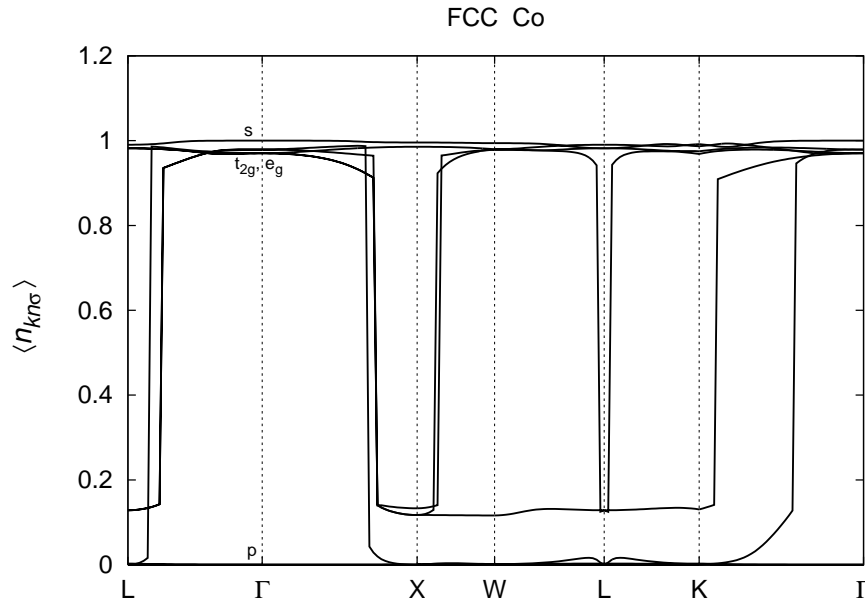


Fig. 19. Momentum distribution functions  $\langle n_{kn\sigma} \rangle$  along high symmetry lines for fcc Co.

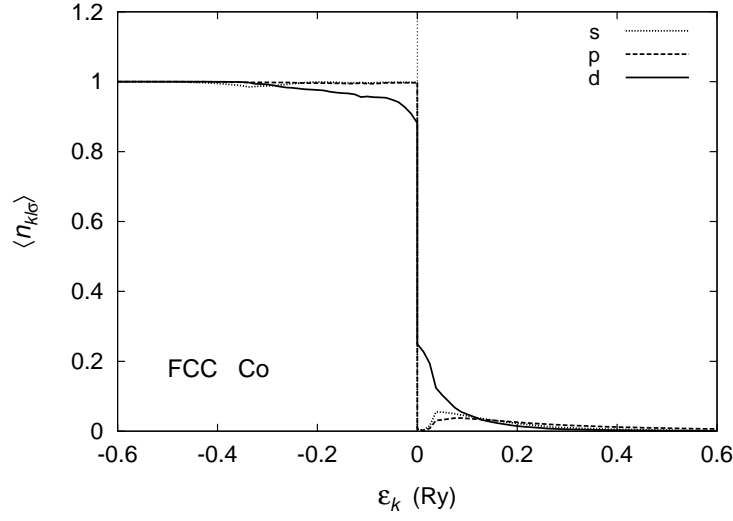


Fig. 20. The projected MDF  $\langle n_{kl\sigma} \rangle$  as a function of the energy for fcc Co. Dotted curve: the MDF for  $s$  electrons, dashed curve: the MDF for  $p$  electrons, solid curve: the MDF for  $d$  electrons.

The  $sp$  bands on the other hand are located far below and above  $\epsilon_F$ .

Figure 22 shows the MDF for fcc Ni. We also calculated the MDF with use of  $U = 0.2205$  Ry and  $J = 0.0662$  Ry adopted by Anisimov *et al.*<sup>44)</sup> (see the dotted curves). We find that the difference between the two results is small. Because of the band structure mentioned above, the MDF of fcc Ni at point  $\Gamma$  takes the values close to 1 or 0: 1.000 for  $s$ , 0.994 for  $e_g$ , 0.992

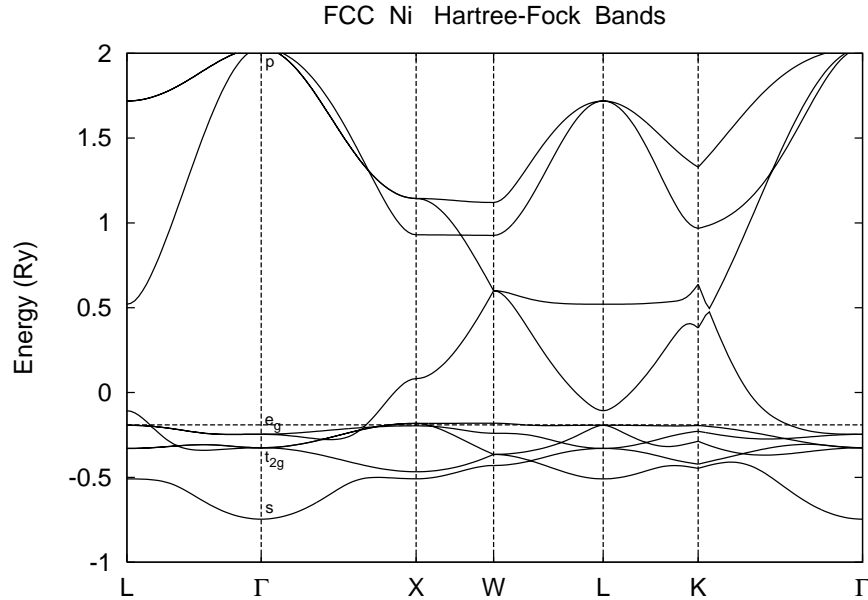


Fig. 21. Hartree-Fock one-electron energy bands of fcc Ni along high-symmetry lines. The Fermi level ( $-0.1903$  Ry) is expressed by the horizontal dashed line.



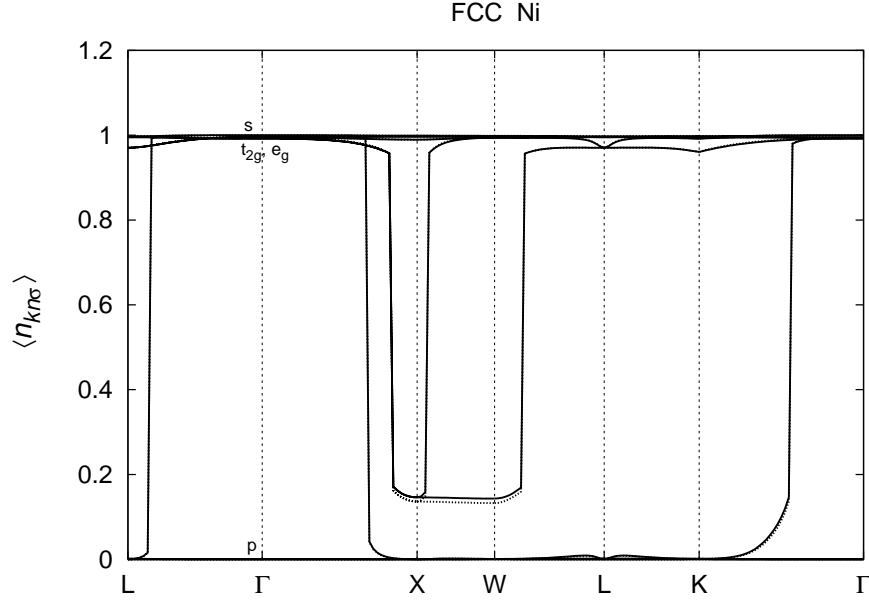


Fig. 22. Momentum distribution functions  $\langle n_{kn\sigma} \rangle$  along high-symmetry lines for fcc Ni. Dotted curves are the result with use of  $U = 0.2205$  Ry and  $J = 0.0662$  Ry.

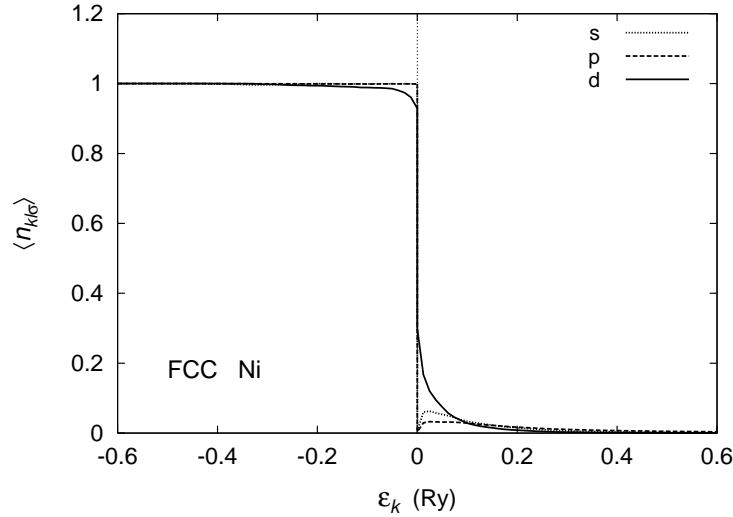


Fig. 23. The projected MDF  $\langle n_{kl\sigma} \rangle$  as a function of the energy  $\epsilon_k$  for fcc Ni. Dotted curve: the MDF for  $s$  electrons, dashed curve: the MDF for  $p$  electrons, solid curve: the MDF for  $d$  electrons.

for  $t_{2g}$ , and 0.000 for  $p$  symmetry electrons. The MDF for  $e_g$  electrons splits into two branches along the  $\Gamma$ -X line. The first branch hardly changes with the change of  $\mathbf{k}$  and takes the value 0.990 at point X. The second one also hardly shows the  $\mathbf{k}$  dependence, but it jumps down at  $\mathbf{k}_F = (0, 0.68, 0)$  and becomes zero at point X.

The MDF for  $t_{2g}$  electrons also splits into two branches when the wavevector  $\mathbf{k}$  moves

to point X. The branch with  $xy$  symmetry remains unchanged and has a value 0.996 at point X. The second branch monotonically decreases with increasing  $|\mathbf{k}|$  along the  $\Gamma$ -X line. It jumps down at  $\mathbf{k}_F = (0, 0.83, 0)$ , and takes a value 0.146 at point X. We find considerably large deviations from the FDF for  $t_{2g}$  electrons along the X-W-L-K line as expected from the energy band structure. In particular, the  $t_{2g}$  flat energy band just above  $\epsilon_F$  on the X-W line causes a large deviation of the MDF. Accordingly, the projected MDF for  $d$  electrons just above  $\epsilon_F$  shows a large deviation from the FDF as shown in Fig. 23. A deviation from the FDF is also found above  $\epsilon_F$  for  $s$  and  $p$  electrons due to hybridization with  $d$  electrons.

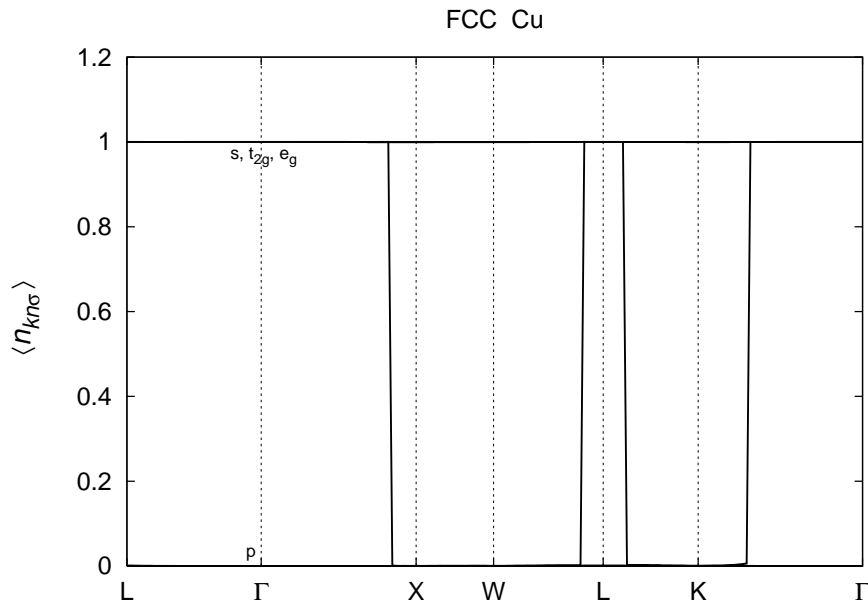


Fig. 24. Momentum distribution functions  $\langle n_{k n \sigma} \rangle$  along high-symmetry lines for fcc Cu.

Finally we present in Fig. 24 the MDF for Cu along high-symmetry lines. The  $d$  bands of Cu are located far below the Fermi level, thus the MDF follow the FDF except a tiny deviation of the branch for hybridized  $pd$  electrons near  $\mathbf{k}_F = (0, 0.52, 0.52)$  on the K- $\Gamma$  line. The MDF of the conduction bands in Cu are described well by the band theory.

### 3.2 Mass enhancement factors

The jump of the MDF on the Fermi surface provides us with the quasiparticle weight, thus the mass enhancement factor. We summarize in Fig. 25 systematic change of calculated partial mass enhancement factors (MEF)  $m_l^*/m$  ( $l = s, p$ , and  $d$ ). The deviations of the partial MEF for  $s$  electrons from the Hartree-Fock value ( $= 1$ ) are only less than 1.5 % from Sc to Cu; the  $s$  electrons do not cause the mass enhancement. The partial MEF for  $p$  electrons are also close to one, though we find 3 ~ 5 % deviation from 1 for the elements from Sc to

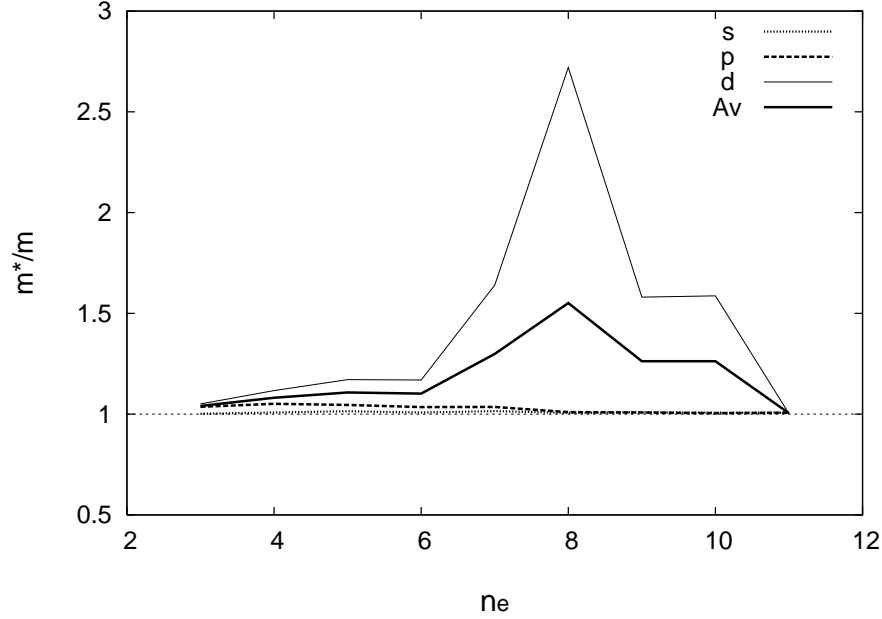


Fig. 25. Partial mass enhancement factors  $m_l^*/m$  ( $l = s, p$ , and  $d$ ) from Sc to Cu as a function of conduction electron number  $n_e$ . Dotted curve: the MDF for  $l = s$ , dashed curve: the MDF for  $l = p$ , the thin solid curve: the MDF for  $l = d$ , solid curve: the average MDF  $m^*/m$ .

Table V. Calculated average mass enhancement factors in iron-group transition metals. The results with parentheses for Fe and Ni are obtained with use of  $(U, J) = (0.1691, 0.0662)$  Ry and  $(0.2205, 0.0662)$  Ry,<sup>44)</sup> respectively.

| Element | Sc    | Ti    | V     | Cr    | Mn    | Fe            | Co    | Ni            | Cu    |
|---------|-------|-------|-------|-------|-------|---------------|-------|---------------|-------|
| $m^*/m$ | 1.040 | 1.081 | 1.108 | 1.102 | 1.299 | 1.551 (1.648) | 1.262 | 1.262 (1.248) | 1.004 |

Mn due to hybridization with  $d$  electrons. The partial MEF for  $d$  electrons show a significant deviation from the Hartree-Fock value except Sc and Cu in which the  $d$  bands are located above or below the Fermi level  $\epsilon_F$ ;  $m_d^*/m = 1.117$  (fcc Ti), 1.171 (bcc V), 1.170 (bcc Cr), 1.640 (fcc Mn), 2.720 (bcc Fe), 1.581 (fcc Co), 1.587 (fcc Ni). In particular,  $m_d^*/m$  for bcc Fe shows the maximum value 2.720 because the narrow  $e_g$  bands are located on the Fermi level  $\epsilon_F$ . The  $d$  electron contribution therefore determines the systematic change of the average mass enhancement  $m^*/m$  via the relation  $m/m^* = D^{-1} \sum_l (2l+1) m/m_l^*$  (see Eq. (25)). We summarize in Table V the average MEF from Sc to Cu. A large value of bcc Fe is caused by the narrow  $e_g$  bands on  $\epsilon_F$ . We also calculated the MEF for fcc Fe:  $m^*/m = 1.349$ . It is smaller than the bcc case since there are no clear flat  $d$  bands on  $\epsilon_F$ .

We examined the origin of the mass enhancement by considering three types of correla-

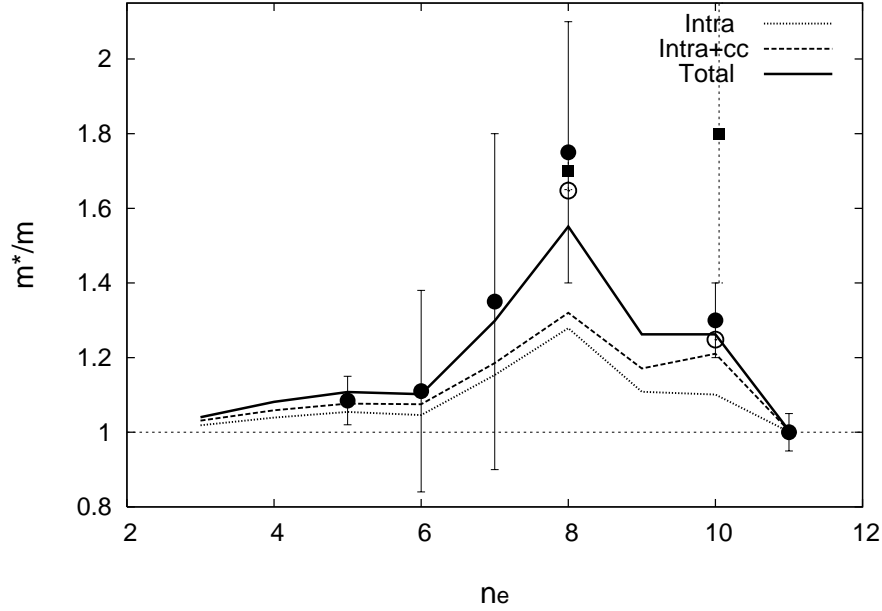


Fig. 26. Calculated mass enhancement factors ( $m^*/m$ ) with/without three type of correlations as a function of conduction electron number  $n_e$ . Dotted line: Intraorbital contribution, dashed line: intraatomic and interorbital charge-charge contributions, solid line: total mass enhancement including interorbital spin-spin contribution. The total  $m^*/m$  calculated with use of Anisimov's  $U$  and  $J^{44}$  are also expressed by open circles for Fe ( $n_e = 8$ ) and Ni ( $n_e = 10$ ). Experimental results obtained from the low-temperature specific heats (ARPES) data are shown by closed circles (closed squares).<sup>48–58)</sup>

tion contributions. Figure 26 shows the result of analysis. Here we defined the intra-orbital contribution  $m^*/m(\text{intra})$  by  $m^*/m$  when  $\tilde{\zeta}_{LL'} = \tilde{\xi}_{LL'} = \tilde{\xi}_{tLL'} = 0$ , the inter-orbital charge-charge contribution  $m^*/m(\text{intra+cc})$  by  $m^*/m$  when  $\tilde{\xi}_{LL'} = \tilde{\xi}_{tLL'} = 0$ , and the full value  $m^*/m(\text{total})$  including the inter-orbital spin-spin contribution. The intra-orbital correlations make contribution to  $m^*/m(\text{total})$  by about 50 % irrespective of elements. The inter-orbital charge-charge correlations make a minor contribution for the elements from Ti ( $n_e = 4$ ) to Fe ( $n_e = 8$ ) (see  $m^*/m(\text{intra+cc}) - m^*/m(\text{intra})$ ). In Ni ( $n_e = 10$ ), the charge-charge contribution is enhanced, and becomes comparable to the intra-orbital contribution. The inter-orbital spin-spin contribution (*i.e.*,  $m^*/m(\text{total}) - m^*/m(\text{intra+cc})$ ) is comparable to the charge-charge contribution for the elements from Sc to Cr. It becomes significant for Mn, Fe, and Co. These results indicate that the mass enhancements of Mn and Fe are determined by the spin fluctuations (*i.e.*, the intra-orbital plus inter-orbital spin-spin correlations), while the charge fluctuations (*i.e.*, the intra-orbital plus inter-orbital charge-charge correlations) are important in the case of Ni.

The mass enhancement factor (MEF) of Fe has recently been investigated from the the-

oretical point of view. Sánchez-Barriga *et al.*<sup>33)</sup> performed the three-body theory + LDA-DMFT calculations with use of  $U = 1.5$  eV and  $J = 0.9$  eV, and obtained  $m^*/m = 1.25$  on the  $\Gamma$ -N line, which is too small as compared with the angle resolved photoemission spectroscopy (ARPES) result<sup>33)</sup>  $m^*/m = 1.7$ . Katanin *et al.*<sup>45)</sup> performed the finite-temperature LDA+DMFT calculations with use of the quantum Monte-Carlo technique (QMC) at 1000 K. They obtained  $m_{t_{2g}}^*/m = 1.163$  for  $t_{2g}$  electrons being in agreement with our result  $m_{t_{2g}}^*/m = 1.22$  (see Table II). But the value for  $e_g$  electrons was not obtained because of the non-Fermi liquid behavior due to strong spin fluctuations at finite temperatures, though we obtained  $m_{e_g}^*/m = 1.67$  (see Table I). More recently, Pourovski *et al.*<sup>14)</sup> reported the LDA+DMFT calculations of bcc Fe at 300 K using the continuous-time QMC technique. They obtained the average mass enhancement  $m^*/m \approx 1.577$  being in good agreement with the present result  $m^*/m = 1.551$ .

We note that the first-principles Gutzwiller theory underestimates the mass enhancement factor. The LDA+Gutzwiller calculations by Deng *et al.*<sup>46)</sup> yield a reasonable value  $m^*/m \approx 1.564$ , but they adopted too large a Coulomb interaction parameter  $U = 7.0$  eV. Recent calculations based on the LDA+Gutzwiller theory with reasonable values  $U = 2.5$  eV and  $J = 1.2$  eV result in  $m_{e_g}^*/m \approx 1.08$  for  $e_g$  electrons and  $m_{t_{2g}}^*/m \approx 1.05$  for  $t_{2g}$  electrons.<sup>47)</sup> These values are too small as compared with the present results  $m_{e_g}^*/m = 1.67$  and  $m_{t_{2g}}^*/m = 1.22$  and too small as compared with the ARPES value<sup>33)</sup>  $m^*/m = 1.7$ .

Experimental data obtained by the  $T$ -linear electronic specific heat and the ARPES are also shown in Fig. 26. Experimentally, Sc shows the hcp structure. The MEF of hcp Sc<sup>48)</sup> estimated from the low-temperature specific heat and the density of states at  $\epsilon_F$  is 2.04. This includes the MEF due to electron-phonon interaction,  $1 + \lambda_{ep}$ , where  $\lambda_{ep}$  denotes the electron-phonon coupling constant. A simple way to remove the effect is to measure the  $T$ -linear electronic specific heat above the temperatures larger than the Debye temperature  $\Theta_D$ . Then we obtain the experimental value due to electron correlations<sup>49)</sup>  $m_{\text{expt}}^*/m = 1.44$ . The present result for the fcc Sc is  $m^*/m = 1.040$ , and is smaller than the experimental value 1.44 for the hcp Sc. The titanium also shows the hcp structure. Taking the same step, we find the electronic contribution of the MEF,<sup>50)</sup>  $m_{\text{expt}}^*/m = 1.19$ , which is considerably larger than the present result  $m^*/m = 1.081$  for fcc Ti.

The vanadium shows the bcc structure, so that we can directly compare the present result with the experimental one. The calculated result  $m^*/m = 1.108$  is consistent with  $m_{\text{expt}}^*/m = 1.02 \sim 1.15$  in which the MEF due to  $\lambda_{ep}$  has been eliminated.<sup>50)</sup> The MEF of bcc Cr are estimated from the low-temperature specific heat data and DOS at  $\epsilon_F$ ;<sup>48,51)</sup>  $m_{\text{expt}}^*/m = 0.84 \sim 1.38$ . The MEF due to the electron-phonon interaction are not eliminated there. The calculated result  $m^*/m = 1.102$  is in the range of the experimental values.

The MEF of fcc Mn can be estimated by an extrapolation of the specific heat data for

Mn-Cu alloys;<sup>48,52)</sup>  $m_{\text{expt}}^*/m = 0.9 \sim 1.8$ . The experimental value  $m_{\text{expt}}^*/m = 1.4$  obtained from the high-temperature specific heat of  $\gamma$ -Mn<sup>53)</sup> is also in this range. The present result  $m^*/m = 1.299$  does not contradict with these data.

The MEF of the bcc Fe estimated from the low-temperature specific heats<sup>48,51,54-56)</sup> are  $m_{\text{expt}}^*/m = 1.4 \sim 2.1$ . The present result  $m^*/m = 1.551$  and the result  $m^*/m = 1.648$  obtained with use of Anisimov's  $U$  and  $J$ <sup>44)</sup> are consistent with the experimental data. The result is also consistent with the experimental value  $m_{\text{expt}}^*/m = 1.7$  obtained by ARPES.<sup>33)</sup>

The cobalt shows the hcp structure below 700 K. The MEF of hcp Co estimated from the low temperature specific heat<sup>48)</sup> is 2.3. Using the MEF of electron-phonon coupling<sup>57)</sup>  $1.2 \sim 1.4$ , we find the experimental value  $m_{\text{expt}}^*/m = 1.6 \sim 1.9$ . The present result for fcc Co  $m^*/m = 1.262$  is smaller than the hcp experimental value  $1.6 \sim 1.9$ .

The experimental MEF of fcc Ni estimated from the low-temperature specific heat and the DOS at  $\epsilon_F$ <sup>48)</sup> is 1.7. When we remove the electron-phonon MEF  $1 + \lambda_{ep} \sim 1.3$  estimated from the ARPES,<sup>58)</sup> we find  $m_{\text{expt}}^*/m \approx 1.3$ . The present result  $m^*/m = 1.262$  and the result  $m^*/m = 1.248$  obtained with use of Anisimov's  $U$  and  $J$ <sup>44)</sup> are in agreement with the experimental value 1.3, but is smaller than the values  $1.4 \sim 2.2$  obtained by the ARPES.<sup>58)</sup>

Although the quantitative comparison between the theory and experiments is not easy at the present stage, the present results seem to be consistent with the experimental data. The underestimate of the MEF in Ni in comparison with ARPES data may be attributed to the magnon mass enhancement<sup>2,59,60)</sup> which is not taken into account in the present theory.

#### 4. Summary and discussions

We have investigated the momentum distribution function (MDF) of iron-group transition metals from Sc to Cu on the basis of the first-principles momentum-dependent local ansatz (MLA) wavefunction method, which we recently developed for quantitative calculations of the ground-state properties.

The MDF in the real system depends on the momentum  $\mathbf{k}$  via both the eigenvectors  $u_{Ln\sigma}(\mathbf{k})$  and the energy eigenvalue  $\tilde{\epsilon}_{kn\sigma}$  measured from the Fermi level. We obtained the MDF along high-symmetry lines of the first Brillouin zone, and analyzed them with use of the partial MDF. In iron-group transition metals,  $3d$  correlated electrons play an important role in the MDF. The average Coulomb (exchange) interaction  $U$  ( $J$ ) increases linearly from 0.1 (0.04) Ry to 0.3 (0.07) Ry with increasing conduction electron number  $n_e$  from Sc to Cu, and the  $d$  electron band width gradually decreases from 0.4 Ry to 0.3 Ry. Thus  $d$  electron correlations become important with increasing  $n_e$ . The correlation effects on the MDF however occur via the  $d$  electrons near the Fermi surface. The MDF for Cu therefore behave as an independent electron system because the  $d$  bands are located far below the Fermi level.

We verified that the MDF for Sc follow approximately the Fermi-Dirac distribution function (FDF) for independent electrons. In Ti, V, and Cr, we found small deviations of the MDF

from the FDF along high-symmetry lines. From Mn to Ni, there exist significant deviations of the MDF from the FDF due to electron correlations. In these systems, the MDF for  $d$  electrons show a strong momentum dependence along high-symmetry lines, while those for  $sp$  electrons show small deviations from the FDF via hybridization between  $sp$  and  $d$  electrons.

We found that bcc Fe shows the largest deviation of the MDF from the FDF because the narrow  $e_g$  bands with flat dispersion are located on the Fermi level. Accordingly, the  $d$ -electron partial MDF for bcc Fe shows the strong momentum dependence via the energy  $\epsilon_k$ . We verified that the MDF for fcc Fe shows less deviation from the FDF since there is no such a narrow band on the Fermi level. In the case of Ni, we found that a large deviation of the MDF with  $t_{2g}$  symmetry appears along the X-W line because of the existence of the flat  $t_{2g}$  energy bands on the Fermi level along the line and strong electron correlations.

We obtained the momentum-dependent mass enhancement factors (MEF) from the jump of the MDF at the Fermi surface. Calculated average MEF show considerably large enhancement from Mn to Ni more than 1.2, while the other metals show small enhancement less than 1.2. The results seem to be consistent with the experimental values, though there is an ambiguity in estimating the electronic contributions of MEF from the experimental data. We found that bcc Fe shows the largest MEF  $1.55 \sim 1.65$  due to  $e_g$  electrons with narrow bands on the Fermi level. Calculated MEF for bcc Fe is in good agreement with the recent results based on the LDA+DMFT at finite temperatures as well as the experimental result obtained by ARPES. The MEF in fcc Fe is found to be 1.35 which is smaller than the bcc value. We found that the mass enhancements for Mn, Fe, and Co are mainly caused by spin fluctuations, while the mass enhancement for Ni is caused by charge fluctuations. For the other metals, both spin and charge fluctuations contribute to the small mass enhancements.

In the present calculations, we assumed the paramagnetic state from Sc to Cu, though the transition metals from Cr to Ni show the magnetic order at the ground state. The bcc Fe, for example, shows the ferromagnetism. In the paramagnetic state, the  $t_{2g}$  electron bands are located below the  $e_g$  electron bands by 0.12 Ry. When the bcc Fe is spin polarized, we expect that the weight of  $t_{2g}$  electrons with smaller  $m_{k\sigma}^*/m$  is increased on the Fermi surface as compared with the  $e_g$  electrons due to exchange splitting. Thus the average MEF is expected to be reduced by  $5 \sim 10$  % due to spin polarization.

The second point which we have to remark is that the present theory is based on the single-site approximation (SSA); it does not take into account the nonlocal correlations. Long-range spin fluctuations are known to cause additional magnon mass enhancement,<sup>2)</sup> which can cause the logarithmic divergence in the vicinity of magnetic instability point.

Direct observation of the MDF by means of the energy integration of ARPES data is highly desired in order to verify the quantitative agreement between the theory and experiment. Calculations of the MDF and MEF for Fe, Co, and Ni in the ferromagnetic state and the

development of the theory to the nonlocal case are left for future work towards quantitative understanding of the ground-state properties of iron-group transition metals.

**Acknowledgment**

The authors would like to express their sincere thanks to Prof. P. Fulde for his valuable comments and encouragements to the present work. This work is supported by a Grant-in-Aid for Scientific Research (25400404). Numerical calculations have been partly carried out with use of the facilities of the Supercomputer Center, the Institute for Solid State Physics, the University of Tokyo.



## References

- 1) J. Friedel and C. M. Sayers, J. de Phys. **38**, L-263 (1977), C. M. Sayers, J. Phys. F **7**, 1157 (1977).
- 2) P. Fulde, *Correlated Electrons in Quantum Matter* (World Scientific Pub., Singapore, 2012).
- 3) Y. Kakehashi, *Modern Theory of Magnetism in Metals and Alloys* (Springer Verlag Pub., Berlin, 2013) Chap. 3.
- 4) M. Imada and T. Miyake, J. Phys. Soc. Jpn. **79**, 112001 (2010).
- 5) P. Hohenberg and W. Kohn, *Phys. Rev.* **136**, B864 (1964).
- 6) W. Kohn and L.J. Sham, *Phys. Rev.* **140**, A1133 (1965).
- 7) R. M. Martin, *Electronic Structure: Basic Theory and Practical Methods* (UP, Cambridge, 2008).
- 8) J.F. Janak and A.R. Williams, *Phys. Rev. B* **14**, 4199 (1976).
- 9) J.F. Janak, *Phys. Rev. B* **16**, 255 (1977).
- 10) V.L. Moruzzi, J.F. Janak, and A.R. Williams, *Calculated Electronic Properties of Metals* (Pergamon, New York, 1978).
- 11) U. von Barth and L. Hedin, J. Phys. C **5**, 1629 (1972).
- 12) J.P. Perdew and Y. Wang, *Phys. Rev. B* **33**, 8800 (1986); J. P. Perdew, *Phys. Rev. B* **33**, 8822 (1986); **34**, 7406 (1986).
- 13) P. Bagno, O. Jepsen, and O. Gunnarsson, *Phys. Rev. B* **40**, 1997 (1989).
- 14) L.V. Pourovskii, J. Mravlje, M. Ferrero, O. Parcollet, and I.A. Abrikosov, *Phys. Rev. B* **90**, 155120 (2014).
- 15) M. C. Gutzwiller, *Phys. Rev. Lett.* **10**, 159 (1963).
- 16) M. C. Gutzwiller, *Phys. Rev. A* **134**, 923 (1964); *Phys. Rev. A* **137**, 1726 (1965).
- 17) J. Bünenmann, F. Gebhard, and W. Weber, *Foundation of Phys.* **30**, 2011 (2000).
- 18) J. Bünenmann, arXiv:1207.6456 [cond-mat.str-el] (2012).
- 19) T. Schickling, F. Gebhard, J. Bünenmann, L. Boeri, O.K. Andersen, and W. Weber, *Phys. Rev. Lett.* **108**, 036406 (2012).
- 20) Y. Kakehashi, S. Chandra, D. Rowlands, and M. A. R. Patoary, *Mod. Phys. Lett. B* Vol. **28**, 1430007 (2014).
- 21) G. Kotliar, S.Y. Savrasov, K. Haule, V.S. Oudovenko, O. Parcollet, and C.A. Marianetti, *Rev. Mod. Phys.* **78**, 865 (2006).
- 22) V.I. Anisimov and Yu. A. Izyumov, *Electronic Structure of Strongly Correlated Materials* (Springer, Berlin, 2010).
- 23) Y. Kakehashi, T. Shimabukuro, T. Tamashiro, and T. Nakamura, J. Phys. Soc. Jpn. **77**, 094706 (2008).
- 24) Y. Kakehashi, M.A.R. Patoary, and T. Tamashiro, *Phys. Rev. B* **81**, 245133 (2010).
- 25) Y. Kakehashi and M.A.R. Patoary, J. Phys. Soc. Jpn. **80**, 034706 (2011); *Phys. Rev. B* **83**, 144409 (2011).
- 26) P. Fulde, *Nature Physics* **12**, 106 (2016).
- 27) Y. Kakehashi, T. Shimabukuro, and C. Yasuda, J. Phys. Soc. Jpn. **77**, 114702 (2008).
- 28) M. Atiqur R. Patoary and Y. Kakehashi, J. Phys. Soc. Jpn. **80**, 114708 (2011).
- 29) M. Atiqur R. Patoary and Y. Kakehashi, J. Phys. Soc. Jpn. **82**, 013701 (2013); **82**, 084710 (2013).
- 30) Y. Kakehashi and S. Chandra, J. Phys. Soc. Jpn. **85**, 043707 (2016).
- 31) S. Chandra and Y. Kakehashi, J. Phys. Soc. Jpn. **85**, 064714 (2016).

- 32) Y. Kakehashi and S. Chandra, J. Phys. Soc. Jpn. **85**, 084708 (2016).
- 33) J. Sánchez-Barriga, J. Fink, V. Boni, I. Di Marco, J. Braun, J. Minár, A. Varykhalov, O. Rader, V. Bellini, F. Manghi, H. Ebert, M.I. Katsnelson, A.I. Lichtenstein, O. Eriksson, W. Eberhardt, and H.A. Dürr, Phys. Rev. Lett. **103**, 26720 (2009).
- 34) O.K. Andersen and O. Jepsen, Phys. Rev. Lett. **53**, 2571 (1984).
- 35) O.K. Andersen, O. Jepsen, and D. Glözel, in *Highlights of Condensed-Matter Theory*, edited by F. Bassani, F. Fumi, and M. Tosi (North-Holland, Amsterdam, 1985), p. 59; O.K. Andersen, O. Jepsen, and M. Sob, in *Electronic Band Structure and its Applications*, ed. M. Yussouff (Springer Lecture Notes, 1987), p. 1; O.K. Andersen, O. Jepsen, and G. Krier, in *Methods of Electronic Structure Calculations* (World Scientific, Singapore, 1994), p. 63.
- 36) G. Stollhoff and P. Fulde, Z. Phys. B **26**, 257 (1977).
- 37) G. Stollhoff and P. Fulde, Z. Phys. B **29**, 231 (1978).
- 38) G. Stollhoff and P. Fulde, J. Chem. Phys. **73**, 4548 (1980).
- 39) G. Stollhoff and P. Thalmeier, Z. Physik B **43**, 13 (1981).
- 40) A.M. Oleś and G. Stollhoff, Phys. Rev. B **29**, 314 (1984).
- 41) P. Fulde, Y. Kakehashi, G. Stollhoff, *Metallic Magnetism* ed. by Capellmann (Springer-Verlag, Heidelberg, 1987) Chap. 5.
- 42) T. Bandyopadhyay and D.D. Sarma, Phys. Rev. B **39**, 3517 (1989).
- 43) J.B. Mann, Los Alamos Scientific Laboratory Rep. No. LASL-3690 (1967).
- 44) V.I. Anisimov, F. Aryasetiawan, and A.I. Lichtenstein: J. Phys. Condens. Matter **9** (1997) 767.
- 45) A.A. Katanin, A.I. Poteryaev, A.V. Efremov, A.O. Shorikov, S.L. Skornyakov, M.A. Korotin, and V.I. Anisimov, Phys. Rev. B **81**, 045117 (2010).
- 46) Xiao Yu Deng, Lei Wang, Xi Dai, and Zhong Fang, Phys. Rev. B **79**, 075114 (2009).
- 47) Giovanni Borghi, Michele Fabrizio, and Erio Tosatti, Phys. Rev. B **90**, 125102 (2014).
- 48) D.A. Papaconstantopoulos, *Handbook of the Band Structure of Elemental Solids* (Springer, New York, 2015).
- 49) G.S. Knapp and R.W. Jones, Phys. Rev. B **6**, 1761 (1972).
- 50) P.A. Beck and H. Claus, J. Res. Nat. Bur. Stand. A **74A**, 449 (1970).
- 51) C.H. Cheng, C.T. Wei, and P.A. Beck, Phys. Rev. **120**, 426 (1960).
- 52) J.E. Zimmerman and H. Sato, J. Phys. Chem. Solids **4**, 135 (1958).
- 53) R.J. Weiss and K.J. Tauer, J. Phys. Chem. Solids **4**, 135 (1958).
- 54) H. Cho and M. Scheffler, Phys. Rev. B **53**, 10685 (1996).
- 55) L. Chioncel, L. Vitos, I.A. Abrikosov, J. Kollár, M.I. Katsnelson, and A.I. Lichtenstein, Phys. Rev. B **67**, 235106 (2003).
- 56) W. Pepperhoff and M. Acet, *Constitution and Magnetism of Iron and its Alloys* (Springer, Heidelberg, 2001).
- 57) T. Jarlborg, arXiv:0208424v1 [cond-mat.str-el] (2002).
- 58) M. Higashimachi, K. Shimada, K. Nishiura, X. Cui, H. Namatame, and M. Taniguchi, Phys. Rev. B **72**, 214438 (2005).
- 59) P. Fulde and J. Jensen, Phys. Rev. B **27**, 4085 (1983).
- 60) A. Hofmann, X.Y. Cui, J. Schäfer, S. Meyer, P. Höpfer, C. Blumenstein, M. Paul, L. Patthey, E. Rotenberg, J. Bünemann, F. Gebhard, T. Ohm, W. Weber, and R. Claessen, Phys. Rev. Lett. **102**,

